The Pennsylvania State University
The Graduate School

FABRICATION AND CHARACTERIZATION OF A LARGE-ARRAY SURFACE-MOUNT HOT-FILM

A Thesis in
Aerospace Engineering
by
Sean Jersey Wang

Submitted in Partial Fulfillment
of the Requirements
for the Degree of

Master of Science

May 2023

The thesis of Sean Jersey Wang was reviewed and approved by the following:

Mark A. Miller
Professor of Aerospace Engineering
Thesis Advisor

Amy Pritchett
Department Head of Aerospace Engineering

Tamy Guimarães
Professor of Mechanical Engineering

Xin Ning
Professor of Aerospace Engineering

Abstract

A surface-mounted hot-film is a thin, flexible resistive sensor that can be used to measure the velocity, wall shear stress, or temperature in a flow. The flexible and compact nature of hot-films combined with their broad measurement capabilities make them versatile sensors for measuring flow on a variety of surfaces. This thesis is aimed at developing and characterizing a hot-film array for large-scale applications such as wind turbines and natural laminar flow airfoils.

A fabrication method was created for for a large surface-mounted hot-film array, outlining the steps in the fabrication process and materials used. In addition to fabrication, a characterization of the hot-film response under static and dynamic conditions was also performed. Driving of the hot-film using both a constant current anemometer as well as a constant temperature anemometer was explored, which found that the constant current anemometer was too unreliable and inconsistent for assessment of the flow. An alternative measure of the hot-film output(s) was also explored in the integrated variance of the voltage output, which showed variation due to a change in the flow condition over the sensor. Fluorescent oil-film and particle image velocimetry were used to validate the variance output of the hot-film(s) under static conditions, and confirmed generally that a higher variance value, on the order 10^{-4} V, indicated attached or unsteady flow, and lower variance values, 10^{-6} - 10^{-7} V, indicated separated or low velocity flow. Gusting inflow in dynamic testing was used to evaluate the hot-film performance under unsteady conditions, however uncertainties in the dynamic PIV results due to unsteady flow and limited samples did not allow for definitive conclusions to be drawn for the hot-films under unsteady conditions.

Table of Contents

List of Figures

List of Tables

List of Symbols

α	angle of attack
c	chord length
CCA	constant current anemometer
CTA	constant temperature anemometer
LE	leading edge
PIV	particle image velocimetry
R	resistance
Re	Reynolds number
s	arc length
σ	standard deviation
σ^2	variance
T	temperaturex
TE	trailing edge
u	streamwise velocity
u_t	wall-tangential velocity
v	transverse
x/c	non-dimensional chord

Acknowledgments

I would like to express my sincere gratitude to my advisor Dr. Mark Miller for his constant support and guidance. Thank you for your dedication, hard work, and patience, which have meant so much to me throughout this research journey and the pandemic.

Thank you to the faculty, graduate, and undergraduate collaborators who have given their time to support me in this research endeavor, as well as my family and friends for their devoted support and bottomless encouragement.

I would also like acknowledge Dr. Christopher House and the NASA Pennsylvania Space Grant Consortium for their gracious financial support. Any opinions, findings, and conclusions or recommendations expressed in this thesis are those of the author and do not necessarily reflect the views of the NASA Space Grant Consortium.

Chapter 1
Introduction

1.1 Overview of Hot-film Sensors

A hot-film sensor is an instrument used to measure the velocity, temperature, or wall shear stress in a flow. A hot-film sensor typically consists of a small, high aspect ratio rectangular metallic sensing element, usually nickel, platinum, or tungsten, which is designed to be sensitive to heat transfer changes in the surrounding fluid. The ends of the hot-film sensing element are typically connected to copper electrical leads and layered between a backing and protective cover material in order to create a standalone hot-film sensor.

Hot-film sensors are typically very thin in terms of height, typically less than 100 µm, so as to minimally disturb the flow, the total sensor lengths and widths vary widely depending on the application. For example, hot-film probe sensors used to measure turbulence can range on the order of 1 mm x 1 mm in terms of total size(6), conversely the surface-mounted hot-films discussed in this thesis are on the order of 2 cm x 12 cm (including electrical leads) and are even larger when embedded in their respective substrates. The sensing element of the TaoSystems SF9902 sensor used in this thesis is depicted in figure 1.1, which also shows the copper electrical leads.

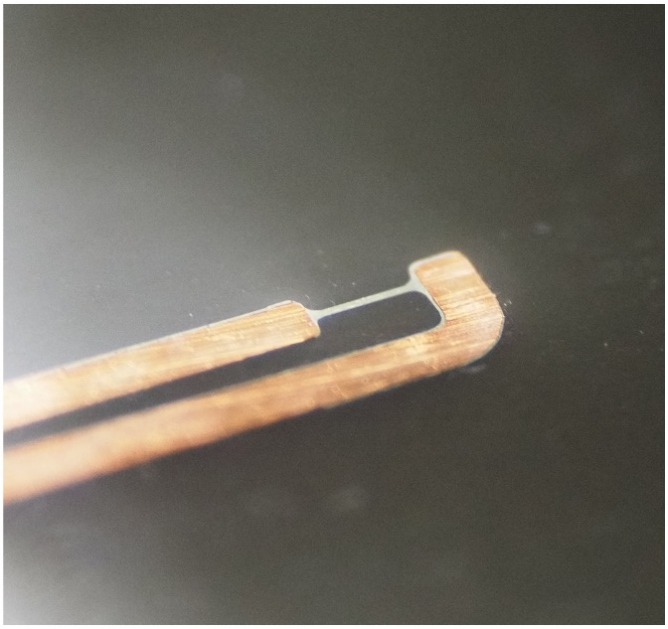

Figure 1.1. The 0.1 mm wide by 1.45 mm long nickel sensing element of the TaoSystems SF9902 hot-film sensor.

In order to make measurements, the hot-film sensing element is heated by an electric current and exposed to fluid flow. The heat provided by the current is taken away by the flow which changes the resistance of the sensing element. The change in resistance of the sensing element can be quantified via the output voltage from a driving circuit and, for a known input current, can be related back to the velocity, temperature, or wall shear stress.

This measurement of a fluid quantity is known as thermal anemometry. This method of anemometry, which uses the heat transfer on a small sensing element, was first developed as early as 1902 (7), which used hot-wire sensors to measure the bulk velocity in a flow. Hot-wires, which are more sensitive and have simpler heat transfer relationships than hot-film sensors, were preferred for early thermal anemometry. It was not until the 1950s and 1960s that hot-film sensors became more commonly used alongside hot-wires due to advancements in the understanding of the underlying heat transfer (8–10). The advantages of hot-films include better durability than a hot-wire, adaptable probe shapes, and lower sensitivity to surface contaminates such as dirt. The primary disadvantage of hot-films is that they are typically less sensitive and have a reduced frequency response compared to hot-wires.

The surface-mounted hot-films discussed in this thesis have features that make them suitable for applications inaccessible by other instrumentation. These features include

flexibility and conform-ability, relatively low cost, large-area coverage potential, and minimal flow disturbance. Comparable sensors have advantages over hot-films, but are not as well suited for the applications of interest, namely large lifting surfaces and surfaces with complex geometries. Hot-wire probes have excellent flow measurement capabilities, but are expensive, fragile, more intrusive to the flow, and only provide point-wise information. Laser Doppler velocimetry and particle image velocimetry systems are sophisticated and non-intrusive, but are expensive, potentially dangerous (due to laser exposure), limited in measurement area, and require comparatively lengthy data processing time. Pressure ports are mechanically simple, but require a large number of ports for sufficient area resolution, are complicated in terms of fabrication, have potentially limited time response, and can suffer from port blockages. Pitot-static tubes are more ubiquitous and readily available than ported lifting surfaces but suffer the same disadvantages as pressure ports in addition to being intrusive to the flow. Thus, surface-mounted hot-films emerge as the best suited instrument for such measurement.

1.2 Driving Circuitry

In addition to the hot-film sensor itself, a driving circuit is required in order to both power the sensor and produce a measurable output voltage for the resulting change in sensor resistance. The two predominant circuit types which were explored were constant current anemometer (CCA) circuits and constant temperature anemometer (CTA) circuits. Both circuits operated the hot-films in a Wheatstone bridge, which enabled finer measurement of small changes in resistance and voltage.

1.2.1 Constant Current Anemometers

In a constant current anemometer (CCA), the input voltage applied to the top of the Wheatstone bridge is kept constant. This produces a stable circuit in which the hot-film sensor is able to function. The CCA circuit is also a very simple circuit compared to the more commonly used constant temperature anemometer, using fewer components and no electronic feedback. The simplicity of the CCA lends itself to scaling up to a large number of acquisition channels, which would be prohibitively expensive using a research grade CTA. The components of the CCA were also low-cost and easily sourced, making in-house fabrication of the circuit easier. The CCA, as tested, was no different than a sensor powered in a Wheatstone bridge. Figure 1.2 shows a simplified diagram of the

core CCA components. In the figure, the hot-film can either be R_2 or R_4. G, nominally a galvanometer, is the measured output of the circuit. In experiments the voltage was acquired from the CCA circuit output.

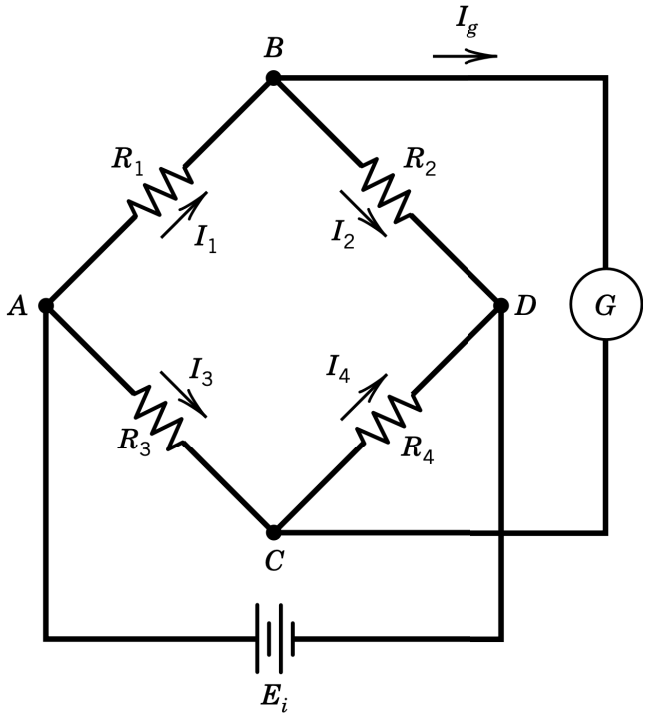

Figure 1.2. A basic diagram of a CCA. Figure reproduced from Figliola and Beasley (1) figure 6.13.

1.2.2 Constant Temperature Anemometers

In a constant temperature anemometer (CTA), sometimes referred to as constant resistance, the temperature at the sensing element is held constant using a feedback loop in the circuit. Electronically, the feedback loop is used to deliver additional current to the hot-film sensor in order to maintain the constant temperature. To provide the feedback, an operational amplifier (op-amp) is used as a differential amplifier to regulate the Wheatstone bridge input voltage based on the output sensor voltage in order to adjust the feedback current. Essentially, the op-amp compares its output with its input and delivers compensatory current as it tries to balance the inverting and non-inverting inputs. The amount of current sent back in the feedback loop is a function of the ratio of resistances between the connected output and input of the operational amplifier. One of these resistors is a load that is typically the hot-film sensor. A basic diagram of a CTA

circuit is shown in figure 1.3. The operational amplifier, labeled differential amplifier in the figure, provides the feedback current to the hot-film sensor, R_D. An off-the-shelf CTA, the TSI IFA-300, was used in the experiments in this thesis in lieu of a custom built circuit, as with the CCA.

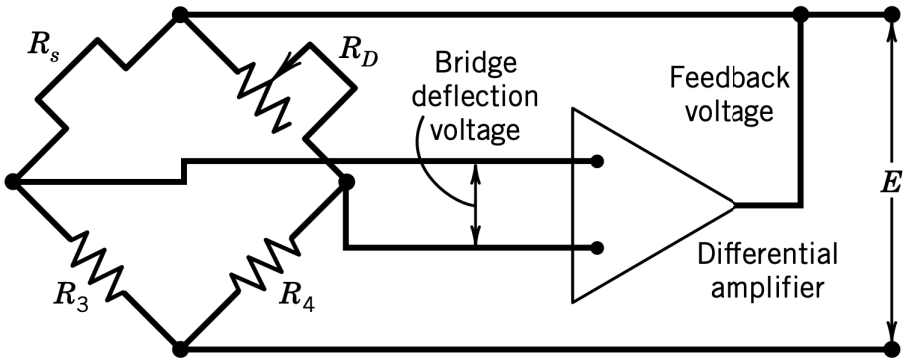

Figure 1.3. A basic diagram of a CTA. Figure reproduced from Figliola and Beasley (1) figure 9.26.

1.3 Applications

Traditionally, due to their durable and flexible nature, surface-mounted hot-films have been used in liquid flows (11), including arterial boundary layer measurement (12), as well as in transonic and sonic flows (13, 14) to characterize transition and separation. Contemporary capabilities of hot-film sensor (and sensor arrays), which are discussed in greater detail in section: Review of Literature, have greatly expanded the number of applications in which hot-film measurement can be useful. More recently, hot-films have been used in new applications which leverage their small size and flexibility. Hot-films have been explored for used on micro air vehicles (MAVs), where conventional instrumentation such as pitot-tubes are both too bulky and heavy. Hot-films have also been explored in respiratory monitoring, as minimally intrusive, wearable sensors that measure the flow below the nose. Conversely, this thesis considers much larger hot-films sensors and potential array setups, for which there are a number applications where they could be used.

1.3.1 Wind Energy

Wind energy is becoming an increasingly prevalent form of clean, renewable energy, particularly as the world transitions to a more sustainable future. With increasing interest in wind energy comes demand for advancements in wind turbine aerodynamic performance, structural lifespan, and aeroacoustics.

Knowledge of the surface flow condition on wind turbines is important for the characterization of rotor blade aerodynamics, including turbulence and its effect on performance and structural fatigue over the turbine azimuth of rotation. The characterization of fatigue in particular has been a point of emphasis in the improvement of wind turbine lifespan, which in turn affects the cost of energy and economic viability. While many computational studies have aided in improving wind turbine design, the challenges associated with large-scale off shore wind farms and turbine noise are underscored by a shortage of experimental validation data. A large, scalable, and conformable sensor, such as a surface-mounted hot-film array, could be a valuable tool in the experimental research of flow and loads over large, geometrically complex wind turbine blades. The scalability of this array would be a key advantageous feature of the sensor, as illustrated in figure 1.4, which shows the relative scales of the area of measurement. Two primary applications of experimental flow characterization were envisioned: analysis of vertical-axis wind turbine loads over their azimuth and analysis of turbulent inflow on large off-shore wind turbines.

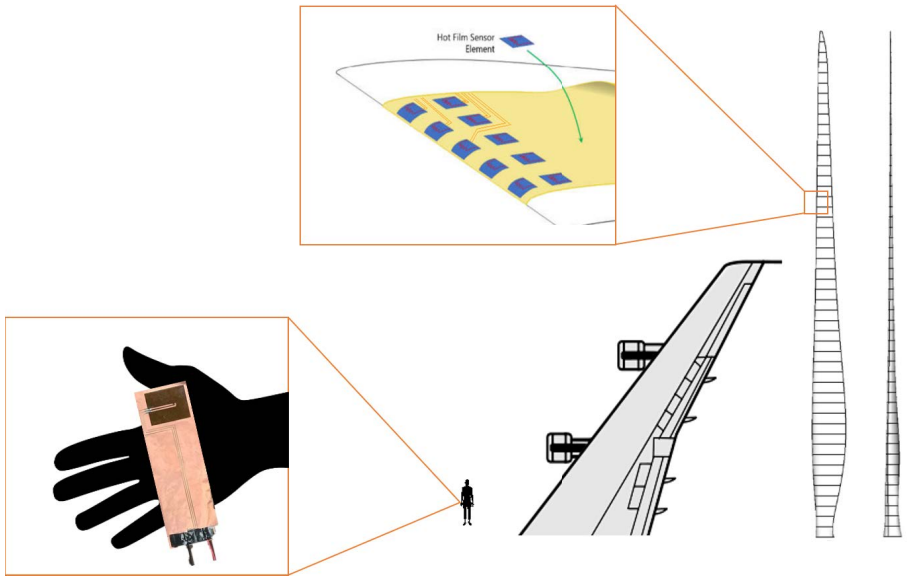

Figure 1.4. The relative physical sizes of a hot-film, hot-film array, and potential surfaces of application. Figure adapted from Buckney et al. (2) figure 3.

Vertical-axis wind turbines are of interest because they experience significant fatigue loading and complex aerodynamics over their azimuth which usually occurs at a relatively high frequency, typically many times per second. This high rotational frequency is necessary for aerodynamic performance, however the repeated cyclic loading is highly detrimental to the lifespan of the turbine. Pitching airfoils are a typically studied proximity to the change in wind direction seen on vertical-axis wind turbines. Pitching airfoils can be readily studied in a laboratory setting (15), however large-scale field measurements would necessitate more complex hardware, potentially including a large-scale hot-film array. Field hot-film measurements would capture as realistic design data as possible, including variables such as weather and unpredictable gusting inflow, which could be challenging to simulate in a laboratory setting. Field data would provide a concrete reference which could aid in the iterative design of future vertical-axis wind turbines.

A similar research goal would be applied to off-shore wind turbines. Large megawatt scale off-shore wind developments are of increasing interest in the U.S., in particular with respect to new sustainability initiatives from the Department of Energy (16), which has the goal of facilitating the deployment of 15 GW of floating offshore wind by 2035. These large-scale, off-shore wind turbines operate in outstandingly harsh environments, which compound existing technical research challenges such as research of off-shore wind farm wakes. A large hot-film array could help aid in the collection of field data, which could include characterizations of flow data at a point in the wind farm, over the turbine blade azimuth, and/or under varying weather conditions. A full-scale sensor array could feasibly be used over a limited area of interest on a full-scale turbine blade, to characterize a specific region of the flow. Or, a scaled-down hot-film array could be used to take measurements in a scaled environment, such as a small field turbine or in a Reynolds-scaled environment, which would similarly produce valuable reference data.

Additional factors such as surface damage and roughness on a turbine blade could also be explored using a large hot-film array. Surface contaminates such as insects and icing, and inherent surface roughness due to blade damage constitute significant performance hits on turbine performance and potential lifespan. Efforts have been made to both diagnose this damage as well as quantify their effects on performance. A hot-film array is potentially suitable for both of these applications, as it would be able to measure the flow quality downstream of potential damage.

Hot-film contributions to the understanding of these turbine characteristics could also indirectly affect wind energy as a whole, not just performance. While wind turbine

aerodynamic performance rightfully has been heavily studied, the long-term success of wind energy also hinges on secondary factors such as aeroacoustics, blade fabrication methods and materials, and economic scaling, all of which would benefit from additional information on experienced fluid interactions as characterized by a hot-film sensor array.

1.3.2 Flow Control

A large hot-film array could also be used to help develop natural laminar flow (NLF) airfoils. Natural laminar flow airfoils are specially designed airfoils whose shape encourages the extension of laminar flow further over the airfoil compared to conventional airfoils. NLF airfoils can be very useful in high endurance aircraft, where efficiency is a primary concern. Significant improvements to aircraft cruise efficiency can also be obtained in the case where the flow is laminar(17). The typical solution for improving cruise efficiency is incorporating active flow control systems, which add weight, cost, and maintenance. NLF airfoils are a passive method for improving efficiency, which helps simplify the design of aircraft.

Typical flow measurement systems are not well suited towards helping develop NLF airfoils, either being intrusive or lacking large-area flow quantification capabilities for NLF airfoils with both large chords and large spans. Common measurement instruments include pitot-tubes and pressure ports, however the former disturbs the flow and only provides point-wise information, while the latter is only suitable in a laboratory setting in quantifying large areas. Surface-mounted hot-films would provide a good compromise in terms of measurement capabilities, being thin enough to minimally disturb while collecting data at many points along the airfoil chord and span, which could be up to meters by meters in scale. Information from surface-mounted hot-films would map the surface condition over the airfoil and provide a relatively straightforward method for confirming and/or characterizing the bulk flow properties. The hot-film array can be combined with specialized lab environments to further reduce complexity as well as potential cost. Scale testing in high pressure, for example, would reproduce the high Reynolds numbers under which NLF airfoils are expected to operate. Information of the surface condition collected by the array can help aid in the development of full-scale models, reproducing phenomena at scale at relatively low cost and experimental complexity.

Control surfaces and their respective controllers are an active area of research and greatly influence how aircraft fly. High lift devices, for example flaps and slats, actively move during operation. The hot-film array would be able to take measurements and

conform to the actively changing geometry, which would be otherwise impossible with conventional instruments such as a hot-wire or pitot-static tube. Hot-films have already been explored in closed-loop control of the flow over an airfoil such as by Poggie et al. (18), and Chabert et al. (19). The current hot-film array being developed would fulfill this role in a much larger physical scale, such as on the flaps of commercial aircraft, or potentially in the control of wind turbine blades.

Further, analysis of unsteady phenomena such as dynamic stall over a swept wing would be greatly served by a hot-film array, which could characterize the time-varying flow state over the entire wing and inform potential modifications to improve performance.

1.4 Research Objectives

This thesis is aimed at producing a fabrication method for a large hot-film sensor array, outlining the materials needed and the different stages of manufacture, as well as the characterization of the hot-film sensor array, including an assessment of the flow using the hot-film outputs. The viability of the CCA as a driving circuit for the array are evaluated and compared against the CTA, assessing the effectiveness of each versus the complexity of implementation. The quality of both the direct voltage output of the driving circuits and the integrated output are considered, specifically in how the hot-film is able to interpret different flow conditions. A preliminary analysis of the sensor array response to dynamic inflow events is also included. This thesis also incorporates many methods for validating the hot-film results. Namely, a fluorescent oil-film method, particle image velocimetry, and XFOIL are used in combination with the hot-film outputs to assess the flow.

Chapter 2
Review of Literature

2.1 Flow Assessment using Hot-films

There have been many similar explorations in the literature using hot-films in arrays to detect flow condition. While these references cover a variety of applications including measuring different quantities, or detecting a different boundary layer phenomenon, these existing studies are helpful in providing a starting point for the exploration of the hot-film as well as in highlighting some important aspects to using hot-films.

2.1.1 Work by J.P. Stack

Regarding detection of transition, separation, and re-attachment, a tremendous deal of work has been done by J.P. Stack and accompanying authors on CTA-driven "thin-film" arrays. The literature mainly addresses closely spaced linear arrays of hot-films and flow characterization using measurements transformed to the frequency domain.

Stack et al. (14) first discussed methods flow separation detection in 1987, which discussed frequency domain techniques and as well as time-resolved signals from the hot-film as indicators of transition and separation. The study focused on boundary layer behavior in the low Reynolds number range from 50,000 to 300,000 on a NASA LRN(1)-1010 low Reynolds numbers airfoil with a chord length of 15 cm. The experimental parameters were similar to those tested in the Results and Discussion of this thesis. The hot-film sensor array, also referred to by Stack et al. (14) as the thin film array, consisted of 30 individual Nickel films, vacuum deposited on a 0.05 mm substrate which was bonded to an LRN(1)-1010 airfoil model with the sensor array staggered in the streamwise direction on the airfoil upper surface. The hot-film array was tested at between 4° and 8° angle of attack and time-resolved measurements from the hot-film

array were recorded. Because of the very close spacing of the hot-film sensors (0.5 mm) and heat conduction to the airfoil substrate, heated sensing elements were only used every other, or every third hot-film sensor. Results collected showed that the general signal noise, and subsequent signal variance, increased with transitioned, separated, or turbulent flow over nominally attached flow. In the frequency domain, this increase in the noise was represented as an amplification of the frequency amplitudes in the 1.0-2.8 kHz range. A significant result from the direct time signal from the hot-film array is an 180° phase shift in the signal between the two closest hot-film sensors at the points of separation and re-attachment. This phase shift corresponded to a change in the shear stress which occurs across the points of separation and re-attachment. A major result of this paper was a decoupling of detection of flow condition with the a velocity calibration. The method only relies on relative changes to the hot-film output signals as well as signal changes with respect to other hot-films, the only requisite was to ensure each hot-film in the array had similar sensitivity characteristics.

Further work by Sewall et al. (20) expanded on the hot-film array by specifically examining frequencies in the 1-200 Hz range as well as flow in the transonic region. The tests were conducted in the Langley Transonic Cryogenic Tunnel in order to achieve flight-relevant Mach numbers of $Ma \approx 0.7$. The results corroborate the same 180° phase shift, specifically showing the behavior in the low frequency <200 Hz bandwidth. Additionally, Sewall et al. (20) show that this detection method is also valid for shock-induced separation, with a laminar separation bubble encapsulated by 180° shifts detected by hot-film sensors along the chord. The results from this method were also confirmed using the oil-film method (21), which tracks the surface shear along the airfoil surface, discussed in greater detail in Chapter 4. Stethoscope probing was also employed to empirically observe the reduction in noise past the point of separation, whose location was consistent with that of the 180° phase shift.

Rudmin et al. (22) also built upon results from Stack et al. (14) by using a hot-film array to map the separation location on a NACA 0012 in a 50,000-130,000 Reynolds number range. The approach was focused strictly on a shear stress calibration of the hot-films as well as frequency response characterization in order to detect separated flow in the frequency domain. In measurement, Rudmin et al. (22) was able to identify regions of high broadband fluctuations in the frequency domain as separated or reattached regions of flow, which was similar to the amplification of the frequency amplitudes observed by Stack et al. (14). The separation location can then be determined for different angles of attack and wind speeds in pseudo-static cases. This method of detection of

separation also does not rely on a velocity or shear stress calibration. Heat transfer to the substrate was again significant consideration in the signal processing setup due to conduction to the substrate causing effective signal attenuation of the hot-film sensors output. To compensate for heat transfer to the substrate, single sensor information was augmented by information from neighboring hot-films, specifically relative changes in voltage, in order to maintain hot-film sensitivity. The hot-films in the array were calibrated insofar as to generate the same output for a known condition, and a windowed cross-correlation was generated to quantify relative changes between neighboring hot-films. The cross correlation also helped elicit information about separated flow, with flow separation between hot-films denoted by a large drop in the cross correlation coefficient from around 0.9 to below 0.5, in addition to observable phase reversal in the voltage output. Additionally with regards to separation, Rudmin et al. (22) corroborated the results from Stack et al. (14), namely that there was sharp drop in amplitude in the sensor output at the point of separation, in addition to the already known phase shift in low-frequency signals from the hot-film past the separation location. The turbulent, redeveloping boundary layer was said to be indicated by an increase in the broadband frequencies 1-10,000 Hz, in particular frequencies past 100 Hz, which is consistent with the results in chap. Results and Discussion. As a confirmation of turbulent re-attachment, Rudmin et al. (22) computed the power spectrum of the hot-film sensor and observed the Kolmogorov -5/3 scaling (23).

2.1.2 Other Detection Methods using Hot-films

Additional methods were explored for separation detection, which employed different methods of flow validation and interpretations of the hot-film sensor output. Schreivogel (24) used thermography, an infrared temperature mapping of a surface, in conjunction with hot-film outputs, to develop a method of locating the point of separation in free flight. Thermography was initially used in order to determine the separation location, which was demarcated by a steep decline in the thermographically measured temperature due to a decrease in the surface shear. For a series of thermographic images, concurrent measurements were also taken using a surface-mounted hot-film array. Using both the thermographic images and the measurements from the hot-film array, a calibration was generated by relating the temperature gradient at the point of separation measured by thermography to the output voltages from the hot-films at the same location. Applying thermographic surface shear-to-voltage calibration to the hot-film output produced a quantity that Schreivogel (24) referred to as the quasi wall shear stress (QWSS), which

was effectively used as the wall shear stress. The QWSS was able to be used to create a quantitative criteria for detection of the separation location, which was determined to be the global maximum in root mean squared of the QWSS over the hot-film array measurements.

Hausmann and Schroder (25) used a frequency domain method and hot-film arrays to detect transition in the transonic regime, using both constant temperature and constant current anemometers as driving circuits. The frequency response of the hot-film array was of particular interest because of the exploration of novel durable coatings for hot-film arrays, which could potentially harm the hot-film sensitivity. The experiments were conducted in a trisonic wind tunnel with a set Mach number of $Ma = 0.7$, as well as on an Airbus Beluga and a Mystere Falcon with $Re \in [3.1, 6.1] \times 10^6$ and $Ma \in [0.27, 0.79]$. Hausmann and Schroder (25) used statistics and the distribution of velocities measured by the hot-films, specifically the standard deviation and skewness, in order to determine transition. Hausmann and Schroder (25) stated, "In the transitional state, the intermittent boundary layer alternates between laminar and turbulent state with equal probability, which leads to bimodal probability distribution of the velocity close to the wall" (25, chap.VIIc). Subsequently, in the bi-modal velocity distribution, the skewness determines whether the flow is either more attached or more separated, with the zero crossing of the skewness indicating the center of the transition region. Skewness of the output per sensor position were plotted to determine the location of transition, denoted by a maximum in the skewness followed by a sign change from positive to negative. Using this method, the location of separation was able to be tracked over the hot-film array locations for different conditions tested on the aircraft. The hot-film skewness results were compared against data from a ported airfoil which was also attached to the experimental aircraft, with agreement in the transition locations.

Sturm et al. (26) explored the boundary layer measurement capabilities of a surface-mounted thermal flow sensor. Specifically, this was measuring separation and re-attachment using the direct output of the flow sensor. The sensor contained a heater as well as two thermopiles placed symmetrically from the heater. The presence of a convecting flow caused an asymmetrical heating distribution along the thermopiles, which was related back to the flow velocity. This is referred to as the calometric principle. Buder et al. (27) also employed the calorimetric principle using a micro-electromechanical system (MEMS) sensor which used two hot-wires positioned in a small cavity to sense the velocity over a surface. In either case, the sensors were configured in an array configuration to detect the voltage over an aerodynamic surface.

Sturm et al. (26) measured the boundary layer on a rounded off flat plate using an array of span-wise and stream-wise staggered sensors. Tests were conducted on a flat plate which was exposed to constant velocities for -10° and 20° angle of attack. The voltage difference between the thermopiles was recorded, which were proportionate to the velocity flowing over an individual sensor. The voltage measurements were used to support the argument of pressure-based flow separation corresponding to a decreasing voltage output, which means a lower difference in convection between the two thermopiles. One point of contention was potential re-attachment of flow and recirculation towards the aft portion of the airfoil at higher x/c locations. Sturm et al. (26) investigated the expected laminar separation bubble location based upon Reynolds number ranges and employed tufts to confirm the separation and re-attachment locations. It was found that re-attachment, specifically "back flow" (recirculation), was demarcated with a sharp increase in the standard deviation in the voltage difference measured by the sensors. It was also important to note that in the -10° angle of attack case, flow deflection was recorded at the leading edge which produced zero flow readings from the sensors. While this does not produced direct results of boundary layer measurement, it is a potential factor to remember for future attempts of pure velocity measurement. The results from Buder et al. (27) also confirmed this behavior, measuring a large drop-off in voltage corresponding to separated flow, in addition to voltage increases where the flow re-attached in the downstream hot-wires.

Lee and Basu (15) measured the unsteady boundary layer on an oscillating NACA 0012 using a very closely spaced multiple hot-film sensor (MHFS), operating at relatively low chord Reynolds numbers of 169,000. The MHFS used contained 140 0.2 µm nickel films spaced 1.30 mm apart, placed linearly along the airfoil chord. The first hot-film sensor was placed at the leading-edge stagnation point in order to capture the full range of the boundary layer. For each measurement, only a group of 14 sensors were connected to the multi-channel CTA used for measurement. Measurements in time allowed for a spatial-temporal measurement of the boundary layer on the airfoil. In order to characterize the flow, Lee and Basu (15) used the 180° phase shift phenomenon (PSP) observed by Stack et al. (14) to note separation. The PSP was first used with a stationary airfoil to map out lines of constant separation over the airfoil s/c for different angles of attack, which produced a static reference. In addition to the PSP, Lee and Basu (15) remarked that variations in the sensor outputs as well as frequency content could also be used to detect transition or turbulent. Lee and Basu (15) specifically noted that close spacing of affected the spatial resolution in detecting the location of turbulent

reattachment and onset of turbulent flow reversal, which was non-ideally resolved with the MHFS. For oscillatory tests, a reduced frequency of $k = 0.109$ was chosen for the same $Re = 169,000$. The airfoil was oscillated in either a 7.5° arc around 0°, or in a 7° arc around 7.5° for $k = 0.109$. In either case the direct signal PSP was detectable in time over sensors along the chord. The same regions demarcated as transitioned or turbulent along the chord displayed a higher level of noise and unsteadiness, which was consistent with the results by Stack et al. (14). Movement of the laminar separation bubble was also observed, which may be pertinent for the unsteady experiments conducted in this thesis. Lee and Basu (15) noted, "the laminar separation and transition were delayed with increasing α, and the reattachment and relaminarization were promoted with decreasing α" (15, sec. 3.2.2). The skewness in the lines of separation due to the hysteresis between upstroke and downstroke was observable in the time trace output of the hot-film array, and was larger in the cases of lower amplitude of airfoil oscillation.

2.2 Heat Transfer

Heat transfer was important in the development of the hot-film array due to the resistive heating nature of the sensing element, specifically in the potential thermal interaction of the hot-film with the substrate and neighboring sensors, and changing ambient temperature. Temperature drift refers to a variation of the hot-film voltage output due to a change in the ambient temperature. For circuits without feedback such as the CCA, the the output voltage of hot-film was found to significantly change with the ambient temperature. In a similar sense to temperature drift, heat transfer via interactions between hot-films could also erroneously affect the measured voltage by the hot-films and were also considered.

2.2.1 Single Sensor Corrections

The traditional hot-wire and hot-film temperature correction for constant temperature anemometers consist of an exponential of the form

$$E_{corr} = \left(\frac{T_w - T_0}{T_w - T_a}\right)^{0.5} \cdot E_a \tag{2.1}$$

derived originally by King (28) and re-expressed by Bruun (6), Jørgensen (29), where E_a is the acquired voltage, T_w is the working temperature, T_0 is the reference temperature, and T_a is the ambient temperature. The correction, often referred to as King's law, was

derived under the assumptions of inviscid, incompressible flow, constant heat conductivity, constant temperature along the length of the wire, and uniform cylindrical cooling.

The temperature correction was attempted for a hot-film operated using a CCA, however the correction did not shift the output curves significantly for given resistances. This was assumed to be due to breakdown of the physical assumptions, including changes to the fluid properties due to changing temperature.

Naturally, the literature was explored for a heat transfer correction derived specifically for constant current anemometers. Hultmark and Smits (30) derived a drift compensation for constant current and constant temperature anemometer driven hot-wires, which used the Joule heating and convective heat transfer equations. The derivations assumed a linear scaling relationship between the sensor resistance and temperature, eq. 2.2, which was a typical assumption for both hot-wires and hot-films. In addition, the hot-wire l/d > 200 (length over diameter) was assumed in order to neglect free convection. As well, relatively large ambient temperature changes, on order of 9 to 15°C, were assumed by nature of the shifts required for changes in the fluid properties.

$$R = R_r(1 + \alpha(T - T_r)) \tag{2.2}$$

Here R is the operating resistance of the hot-wire, R_r is a reference resistance, α is the temperature coefficient of resistivity, and $T = T_w$ and T_r are the working temperature and reference resistances respectively. Eq. 2.2 was re-written as Eq. 2.3 and combined with the assumed form of ΔT in eq. 2.4 to derive the final temperature correction, eq. 2.5.

$$T_w - T_r = \frac{1}{\alpha}\left(\frac{R}{R_r} - 1\right) \tag{2.3}$$

$$\Delta T = (T_w - T_a) = (T_w - T_r) + (T_r - T_a) \tag{2.4}$$

$$\Delta T = \frac{1}{\alpha}\left(\frac{E}{IR_r} - 1\right) + (T_r - T_a) \tag{2.5}$$

In eq. 2.5, E is the output voltage of the sensor. This temperature correction was combined with the calibration equation obtained by Hultmark and Smits (30), eq. 2.7, which was derived by equating the Joule heating and convection, eq. 2.6, and manipulating the Nusselt number, Nu.

$$EI = h\Delta TA = \frac{kNu}{d}A\Delta T \tag{2.6}$$

$$\frac{U}{\nu} = g_3\left(\frac{E}{k\Delta T}\right)) \tag{2.7}$$

Here, I is the current through the wire, h is the convective heat transfer coefficient, A is the wire surface area, d is the diameter of the wire, k is the thermal conductivity of the wire, and Nu is the Nusselt number, $Nu = \frac{hd}{k} \approx g(Re)$. The Nusselt number was manipulated to obtain the calibration relationship between the velocity and the output voltage, and was assumed to only be a function of the Reynolds Number, Re.

Hultmark and Smits (30) found that the temperature correction, in combination with the velocity calibration, produced highly accurate results with a coefficients of determination values of R^2 of 0.9998 and 0.9997 for two cases tested. In addition, the CCA correction was attempted for the hot-wire operating under constant temperature mode, and the R^2 was found to 0.9991, still very accurate.

Temperature corrections were ultimately not applied to the hot-films used in this thesis for three reasons: 1, the high uncertainty in the measured temperatures during data acquisition, and 2, a potential breakdown in assumptions due to using a hot-film, and 3, the decision to use the simpler calibration-less flow detection method developed by Stack et al. (14).

2.2.2 Thermal Considerations for an Array

Because the hot-films of interest were surface mounted to both the airfoil and in relatively close proximity to one another, thermal conduction to the host surface and downstream convective were also reviewed to see what effects the substrate and neighboring hot-films could have on measurements.

Sun et al. (31) proposed a diffusive heat equation model for handling downstream convection of heat from hot-film sensors and conduction to the array substrate. Here, Sun et al. (31) described conduction to the wall as 1-dimensional diffusive heat transfer, eq. 2.8. The convective heat transfer due to the flow was written as the convective heat transfer equation, ignoring changing temperature with time and the wall normal velocity, eq. 2.9.

$$k_s t\frac{\partial^2 T_s}{\partial x^2} + k\frac{\partial T}{\partial y}|_{y=0} = 0 \tag{2.8}$$

$$u\frac{\partial T}{\partial x} = \alpha\frac{\partial^2 T}{\partial x^2} + \frac{\partial^2 T}{\partial y^2} \tag{2.9}$$

where T is the temperature, u is the streamwise velocity, α is the thermal diffusivity, k is the thermal conductivity, and subscript s denotes substrate quantities as opposed to sensing element quantities.

Sun et al. (31) used eq. 2.8 and 2.9 to simulate heat transfer on a model airfoil of interest for both air and water to examine thermal affects on a hot-film sensor array. In air, for a velocity of 22 m/s and a hot-film working temperature of 85°, the minimum spacing to avoid crosstalk was 11.33 mm. In water, for a velocity of 0.5 m/s and a hot-film working temperature of 45°, the minimum spacing to avoid crosstalk was 5.95 mm. These results were verified using both wind tunnel and water channel experiments, which confirm spacing $6mm \leq S \leq 12mm$ and $S < 6mm$ for air and water respectively. For similar overheats, these spacing requirements were easily met for experiments conducted in this thesis.

2.3 Particle Image Velocimetry

Particle image velocimetry (PIV) aided in the validation of hot-film sensor data by providing snapshots of the bulk flow conditions during the experiments. Planar PIV, shortened to just PIV, was used for validation and consisted of a single laser-illuminated sheet of particles from which images were captured and vector fields were generated. There were many aspects of the PIV setup which needed to be considered, including mitigation of surface reflections, processing velocity data, and predicting of transition and separation.

In PIV, surface reflections caused a loss of vector information near the surface because the near-surface tracer particles are no longer able to be identified due to the high light intensity from the reflections. Because the flow measured by the hot-films was in the region close to the airfoil surface, surface reflections were a significant factor in the sensor characterization. Paterna et al. (5) examined different surface treatments and their effectiveness in mitigating surface reflections. Paterna et al. (5) examined three categories of materials, absorbing materials, reflecting materials, and transmitting materials. Sample materials included flat black and fluorescent painted woods, glass and acrylic mirrors, polished metals, and float and acrylic glasses. In the study, a 527 nm laser sheet was emitted onto a sample material and images of the reflection, which were later averaged, were captured using an off-angle camera. The intensity of surface reflections for a given material were assessed by both the peak light intensity as well as the average light intensity from the averaged images. It was found that the fluorescent fluorescent

painted wood, mirrors, and glasses resulted in both relatively low average and peak light intensities. The whole table is shown in table 2.1, below.

Table 2.1. Tabulated average and peak light intensities for reflections off variety of surface finishes. Table reproduced from Paterna et al. (5) table 1.

		Light intensity		Reflection reduction
	Laser power	Average (counts)	Peak (counts)	coefficient
Absorbing materials				
A1 flat black painted wood	30%	1351	>4095	1.0
A2 flat black LEGO plate	30%	1240	>4095	1.1
A3 black cardboard	30%	1337	>4095	1.0
A4 black PE-coated tape	30%	1091	4092	1.2
A5 black vinyl sheet	30%	935	2910	1.4
A6.a fluorescent paint (+35%)	30%	285 (385)	3325 (4489)	4.7 (3.5)
A6.b fluorescent paint (+35%)	80%	60 (81)	344 (464)	22.5 (16.7)
Reflecting materials				
R1 first surface mirror ($Ra < 50$ nm)	30%	72	2069	18.8
R2 glass mirror ($Ra < 50$ nm)	30%	64	151	21.1
R3 acrylic mirror ($Ra < 50$ nm)	30%	635	3278	2.1
R4 grinded steel ($Ra = 580$ nm)	30%	1306	4051	1.0
R5 electropolished steel ($Ra = 200$ nm)	30%	187	2458	7.2
R6 multiple-polished steel parallel ($Ra = 50$ nm)	30%	805	>4095	1.7
R7 multiple-polished steel perpendicular ($Ra = 50$ nm)	30%	334	1577	4
R8 polished aluminum ($Ra = 70$ nm)	30%	429	4042	3.1
Transmitting materials				
T1 float glass 2 mm ($Ra < 50$ nm)	30%	44	104	30.7
T2 float glass 5 mm ($Ra < 50$ nm)	30%	46	503	29.4
T3 acrylic glass 2 mm ($Ra < 50$ nm)	30%	118	352	11.4

PIV was also explored to see if it was feasible for direct detection of separation via the velocities. Burgmann et al. (32) used both high speed time-resolved planar PIV in addition to stereo-scanning PIV in water in order to determine the separation location, and more broadly the location of the separation bubble, on a SD7003 airfoil. The planar PIV was performed in a plane wall-normal to the airfoil surface at several locations along the airfoil span to obtain coarse span-wise flow information. The stereo-scanning PIV was performed on parallel laser planes over the airfoil surface. The number of laser planes varied from 5 to 6 planes, with the closest plane positioned approximately 0.5 mm to the airfoil surface and subsequent parallel planes spaced 1 mm apart. By combining these methods, pseudo-volumetric velocity data was able to be collected. Burgmann et al. (32) was able to use the PIV data to detect both the separation and re-attachment locations by analysis of the particle streamlines. By examining the streamlines and the averaged particle traces, "Near the separation point the deviation of these traces from the airfoil surface [was] quite evident" (32, chap 3.1), and was interpreted to mean the location where calculated dividing streamline re-attached to the airfoil surface. The point

of re-attachment was taken to be the point where the dividing streamline closed back to the airfoil surface. Because of the reliance on individual particle streamlines, detection of separation and re-attachment were only possible using high-speed, time-resolved PIV. Although the PIV setup used in this work was not a time-resolved system, the literature was still used as a methodological supplement insofar as approximate indicators in the flow are concerned, such as approximate streamline behavior in the separation bubble, which could be used as a reference to interpret the hot-film sensor data.

Analysis of the boundary layer for the purposes of estimating transition using PIV has also been explored in the literature. Park et al. (33) examined both the near-wall velocity profiles as well as the root mean squared (RMS) velocities in the regions above the boundary layer to determine separation and transition locations, respectively. The study was also interested in the capabilities of PIV in measuring the laminar separation bubble. Park et al. (33) performed stream-wise, wall-normal PIV experiments to image the boundary layer statically on a DAE51 airfoil at 39,000 to 118,000 Reynolds number. In order to properly resolve the velocity profiles, several smaller interrogation regions were imaged along the surface of the airfoil, then stitched back together to recover a continuous averaged vector field. The points of separation were determined classically using the resolved velocity profiles, with the inflection point signifying separation. The RMS velocities of the vector fields were processed to explore possible criteria for identifying transition. It was found that the region of amplified RMS occurs twice, once near the point of separation and another in a region far downstream of the point of separation. The region far downstream was attributed to accelerated mixing of the shear layer and did not contain the point of separation. The upstream region of RMS amplification was studied by comparing the RMS velocity and mean velocity profiles in the region, and it was found that a large increase in the normalized stream-wise RMS velocity corresponded to the location of the inflection point in the mean velocity profile. This behavior was also observed in results by Wynnychuk and Yarusevych (34), where both PIV and thermography were used. Further exploring RMS velocity behavior, Park et al. (33) found that transition could be detected by sharp increase in the transverse RMS velocity, which can be observed to change over the airfoil x/c. Because the region of transition was qualitatively defined by a sharp linear increase in the transverse RMS velocity as a function of x/c, Park et al. (33) note that potentially uncertainty needs to be accounted for in this area of transition, and thus calculated an approximate uncertainty of $\Delta(x/c) \approx \pm 0.02$. Park et al. (33) also found, "The rapid amplification of the RMS value for both velocity components was clearly observed and centered at the inflection point of

the averaged velocity profile" (33, sec. conclusion). Suggesting the separation location could be potentially be estimated near the region of RMS amplification even where the near wall velocity profiles are not well resolved, under the assumption Kelvin-Helmoltz instabilities are responsible for transition.

2.4 Hot-film Array Motivation

Hausmann and Schroder (25) applied their previous discussed transition detection methodology to a hot-film array that was adhered to the wing on an Airbus Beluga and a Mystere Falcon. The hot-film arrays contained densely clustered sensors and were wrapped around the leading edge of the wings. Different coatings were applied to multiple hot-film arrays to assess the durability of the different arrays. The hot-film arrays measured the voltage output to detect transition. A similar goal was envisioned the for the hot-film array fabricated in this thesis, where both the fabrication method and measurement capabilities were intended to be evaluated in the context of detecting flow condition. The array fabricated in this thesis was significantly larger that those in previous works by Stack et al. (14), Lee and Basu (15), Rudmin et al. (22), Sun et al. (35).

Preliminary results from Pang et al. (36) suggested superior frequency response with a larger convective heat transfer area in addition to higher sensitivity to due increased thermal mass of the sensing element. These prior works motivated the research questions behind fabrication and testing of the large-array hot-film.

Chapter 3
Hot-film Array Fabrication

3.1 Components

The large-array hot-film consisted of two main parts, the hot-film sensors themselves, containing the nickel sensing element, and a custom etched copper substrate backing, which contained sensor beds for the hot-film sensor and electrical wiring.

The hot-film sensors used in the fabrication of the arrays were commercially available, relatively low-cost TaoSytems Senflex SF9902 sensors. These commercial sensors were pre-made by the manufacturer and used a 0.1 mm wide by 1.45 mm long nickel sensing element with a 6-8 Ω cold resistance, approximate thickness of 50 µm, and maximum current rating of 120 mA. The Senflex SF9902 sensors also contained leads with standard thicknesses of 0.0127 mm (½ mil) and widths of 0.762 mm which connected to the nickel sensing element. A full SF9902 sensor is depicted in figure 3.1, and the hot-film sensing element was seen previously in figure 1.1.

Figure 3.1. Senflex® SF9902 is a single-element hot film sensor on a 120 mm x 20 mm substrate. Figure reproduced from of Systems Integration Inc. (3) pg. 5.

The substrate backings were custom made from plain sheets of copper-clad polyimide film. The copper layer of the copper-clad polyimide was etched to create the design of the hot-film sensor substrate, which accommodated the SF9902 hot-film sensors. The

copper-clad polyimide used in fabrication had a total thickness of approximately 60 µm, the copper itself had an approximate thickness of 50 µm (2.0 mils), and the bare polyimide had an approximate thickness of 5 µm (0.2 mils). The copper layer thickness was chosen such that the SF9902 sensors sat as flush as possible in the etched substrate to minimize the boundary layer disturbance. To etch the copper substrate, ferric chloride, an acidic compound, was used. Ferric chloride was used because it is safe to handle and inexpensive, thus suitable for the anticipated large scale etching.

The creation of the final hot-film array consisted of four main steps: layout design, masking, etching, and assembly.

3.2 Layout design and Masking

Sensor substrate layouts were first designed in Adobe Photoshop using the hot-film dimensions provided by the manufacturer. Elements of the substrate design included portioned areas to act as the sensor beds for the hot-film sensor(s), electrical lead paths for each sensor, and terminal solder pads for external circuitry.

The length, thickness, and path of the substrate electrical leads can affect their resistance. For the relatively short differences in lead length in the test array, lengths between approximately 8.5-10.5 inches, the difference total lead resistance was typically small, within 0.3 Ω. For larger substrate designs, the path of of the substrate leads need to be carefully considered as differences in length between sensor leads can affect the respective sensor response to driving circuitry. The lead resistance can be calculated using the cross-section and resistivity of the lead material, though in fabrication of the scale array no resistance calculation was performed.

The substrate layout designs were generated at a scaling of 300 dots per inch (dpi) to ensure sufficient resolution in the final print. A template which included different components such as sensor cutouts and varying shapes of electrical leads was created to simplify the design process. Once the final design was completed, the design was flipped horizontally and exported as a PNG file in preparation to be printed and used in the dye transfer method.

The substrate layout mask was applied to the substrate using the dye transfer method. The dye transfer method is a method of applying a mask to a host surface, in this case the copper-clad polyimide, by transferring a mask design from a intermediate medium such as toner transfer paper using heat and pressure. First, the substrate design was flipped and printed onto a sheet of toner transfer paper. The substrate layout needed to

be flipped so the design is transferred in the correct orientation on the unetched copper substrate.

To transfer the design onto the copper-clad polyimide, the toner side of the toner transfer paper was interfaced with the copper side of the copper-clad polyimide, then heat and pressure were applied to begin the transfer process. To apply the heat and pressure, a Tamerica SM-330 laminator was used. For lamination, the leading edge of the combined toner transfer paper-unetched substrate sandwich were taped together, and either the toner transfer paper or the unetched substrate were pulled taut while the design was passed through the laminator in order to minimize creasing. Generally, at least three passes were made through the laminator to ensure proper dye transfer. After lamination the toner transfer paper and copper-clad polyimide were rinsed under cold water for around one minute in order for the toner to release and transfer properly. The result of the dye transfer method was a correctly-oriented mask of the substrate design on the unetched copper-clad polyimide. After dye transfer, toner mask was still porous and permeable by the ferric chloride used in etching. Thus, the toner mask needed to be sealed before etching. Toner reactive foil (TRF) was applied to the masked copper-clad polyimide to create an impermeable mask and was applied in exactly the same way as in the dye transfer method. The TRF was interfaced against the masked copper-clad polyimide and passed through a laminator. The heat and pressure from the laminator transferred the sealing material from the TRF to the masked portion of the substrate. The final result was the non-porous masked copper-clad polyimide substrate ready to be etched.

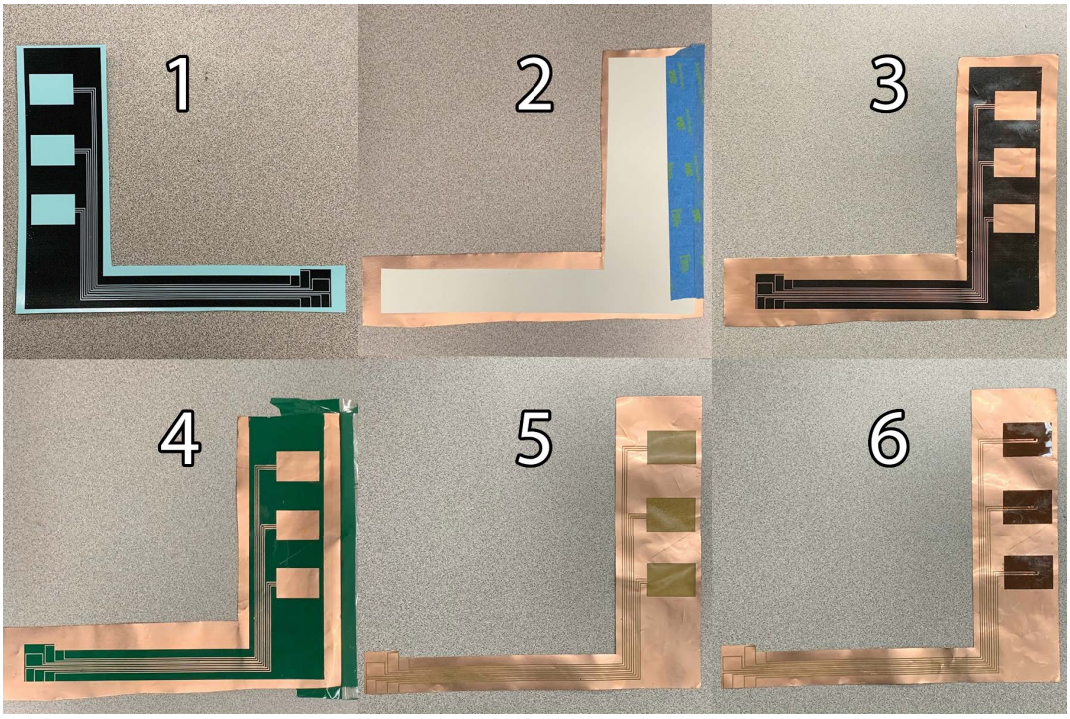

Figure 3.2. The stages of the fabrication process for the array hot-film are shown: steps 1, 2 show the dye transfer process, steps 3, 4 show the bare toner mask as well as the TRF-sealed mask, step 5, 6 show the etched copper substrate without and with the SF9902 sensors attached respectively.

3.3 Etching and Asssembly

To etch the TRF-sealed masked copper-clad polyimide substrate, it was immersed in a ferric chloride solution which etched away the unmasked portions of copper in a series of oxidation-reduction reactions. In the governing chemical reactions, ferric chloride first reacts with the bare copper and creates iron chloride and copper(I) chloride (CuCl). The product copper(I) chloride is then reacted with ferric chloride producing copper(II) chloride ($CuCl_2$). Lastly, the copper(II) chloride reacts with the remaining copper to etch away the substrate.

The etching process can be lengthy depending upon the thickness of the copper in the copper-coated polyimide backings. The thicknesses of copper chosen for sensor substrates, which were approximately 50 µm thick, typically required around 45 minutes to fully etch. Regularly checking on and agitating the ferric chloride and immersed substrate was performed, and is recommended to ensure uniform and uninterrupted etching. Etching was complete when the translucent polyimide backing was plainly visible without any

copper remaining. Once cleaned, the substrate was considered finished and was ready to be bonded with the hot-films to create the final array hot-film.

To bond the SF9902 hot-film sensors to the substrate, an adhesive was applied to the sensor bed, which fit trimmed SF9902 sensor(s). Common commercial adhesives, such as 3M Super 77, were sufficient for adhering the hot-films to the substrate. Electrical continuity was achieved by soldering the substrate and hot-film sensor leads and created the final array hot-film. Affixing the hot-film array to the aerodynamic surface of interest was also done using 3M Super 77. In the cases where structural reinforcement was used, the materials were out of the flow region completely, such as at the airfoil root. The combined hot-film and substrate was designed as a proof of concept with dimensions 2 x 11 " as shown in figure 3.3. Full-scale versions of the hot-film array, which could be scaled up to meter by meter scale for wind turbines or other applications, would use a similar method of fabrication. Modifications to the method of dye transfer and application of etchant would need to be made to accommodate the increased size, such as tiled dye transfer and brushed application of the etchant.

Figure 3.3. Hot-film prototype fabricated for use in experiments attached to an NACA 0012 airfoil. The copper substrate wraps around the leading and trailing edges. Sensor leads are concealed on the opposite surface of the airfoil and extend away from the array towards the airfoil root, where they are connected to driving circuitry.

Chapter 4
Experimental Setup

4.1 Testing Rationale

Characterization of the hot-film sensor required both static and dynamic testing in order to expose the hot-film sensor to various conditions. Static testing was first conducted to generate reference hot-film output values which corresponded to known aerodynamic conditions over the host airfoil, specifically the tests were designed to expose the hot-film was to either attached or separated flow. This was accomplished by varying the angle of attack of the model airfoil and wind speed of the wind tunnel. Dynamic testing was performed to simulate gusting inflow, which tested the hot-film sensor frequency response as well as provided another point of reference for the sensor output to various flow conditions.

Validation methods were also needed to verify the sensor outputs for both static and dynamic testing. The two primary validation methods used were fluorescent oil-film and particle image velocimetry. The hot film array output was captured simultaneously with the validation methods to ensure consistent results. In static testing, the fluorescent oil-film created a visual representation of the surface shear for different experimental parameters, which could be used to diagnose the flow condition at the airfoil chord locations containing the hot-film sensor(s). PIV, used in both static and dynamic tests, produced a two-dimensional vector field in a plane normal to the airfoil surface which could be compared to the hot-film measurements. XFOIL was also used as a supplement to these two validation and consisted primarily of simulations to double check the results from either.

Both the CCA and CTA were tested, however an emphasis was initially placed on testing of the CCA in order to sufficiently explore its sensor driving capabilities. The CCA circuit was tested because it was a relatively low-cost anemometry circuit, used

readily available components, and had a simple component layout. Additionally, the CCA was expected to be more stable as it excluded the electronic feedback mechanism used in the CTA. Thus, if the CCA was able to demonstrate favorable flow detection capabilities, it would be a compelling low-cost, robust solution for surface flow characterization, and for scaling up to the prodigious sizes of wind turbines. Testing of the CCA included the aforementioned static angle of attack and wind speed variation, which was intended to capture a range of sensor-circuit combinations, as well as an examine the frequency domain response as an alternative flow measure, as suggested in the literature (14, 22). Methods of data processing in the frequency domain were also explored because they had the potential to be less sensitive to temperature changes in the flow, unlike the DC voltage output of the CCA, as discussed in 5.4. The time series was transformed to the frequency domain using an FFT algorithm (the pwelch function in Matlab) which computed the power spectral density of the signal as a function of frequency. The frequency spectra was then integrated in the 1-1000 Hz band to yield the portion of the total signal variance within this frequency range. The 1-1000 Hz band was chosen because it contained a majority of the energy in the signal variance, and also because 1000 Hz is the practical upper limit of the CCA circuit frequency response (37). The integrated quantity was referred to as the integrated variance, and used for flow characterization. Ultimately, the CCA circuit did not produce satisfactory results, as the CCA output contained significant noise levels, as detailed in 5. Thus, a decision was made to use a reliable, off-the-shelf, commercial CTA circuit (TSI IFA-300) in place of the CCA for static and dynamic testing.

A number of angle of attack and wind-speed sweeps were performed using the commercial CTA to confirm that it did not suffer from the noise and temperature dependence observed on the CCA-driven array. Additional, dynamic tests were designed to simulate unsteady flow conditions that could potentially be observed on a wind turbine or pitching airfoil. Due to facility limitations, a limited range of Reynolds numbers and gusting frequencies were tested. The Reynolds number was in the range 30,000 to 200,000, and gusting frequencies ranged from 0.05 to 0.5 Hz. It was found from PIV that sinusoidal wind speed variation could produce unsteady flow events, somewhat representative of a pseudo-reduced frequency (38). The hot-film output signal, verified against PIV data, was used to augment the static results to investigate how the signal variance of the hot-film output changed in order of magnitude for different flow conditions.

4.2 Testing Facility

Two separate facilities were used during the testing of the hot-film sensor array and driving circuitry. A large, closed-loop wind tunnel was used only for static testing, and a continuously adjustable open-jet wind tunnel was used both for continued static testing as well as for dynamic testing.

4.2.1 Closed-loop Wind Tunnel

The closed-loop wind tunnel was used for static testing only, which included angle of attack and wind speed variation testing conducted on a pseudo-2D flat plate with a $5\frac{3}{16}$ inch chord (13.18 cm) and 2 ft span. The wind tunnel was a vertical close-looped design with a 110 ft circuit length and a height and width of 14 ft and 10 ft respectively. The dimensions of the closed-throat test section were 2 ft wide by 3 ft tall by 20 ft long. The test section contained a rotary mounting mechanism in order to accommodate airfoils, and was coupled with a gearing mechanism to adjust angle of attack. The contraction area ratio of the wind tunnel was approximately 10:1. The wind tunnel was driven by a 48 in. diameter 25 hp belt-driven fan, and the wind tunnel velocity was manually adjustable between 0-150 ft/s (0-46 m/s). Turbulence management consisted of 5 screens, 1 perforated plate and a 6 in. long 3/8 in. cell size honeycomb section. The nominal turbulence intensity in the center of the test section was a maximum of 0.35% below 20 ft/sec and at 80 ft/sec, and 0.15% between 30 to 60 ft/sec and above 120 ft/sec, values courtesy of Professor Rick Auhl at Penn State. The wind tunnel was equipped with pitot tubes and a type-k thermocouple in order to measure the wind speed and temperature respectively. The wind tunnel schematic is shown in figure 4.1.

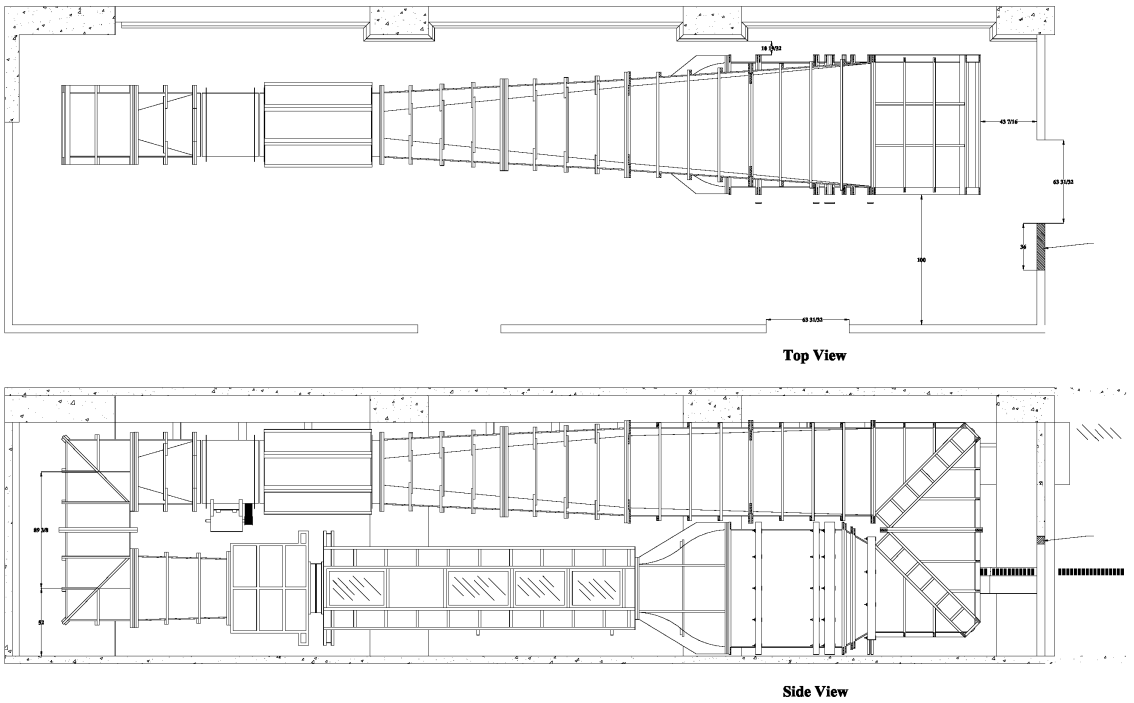

Figure 4.1. Schematic of the closed-loop wind tunnel used for initial static testing. The top and side views are presented as labelled. The flow is from left to right in the top view, and in the clockwise direction in the side view. Drawing courtesy of Brian Kane.

The static testing setup in the closed-looped wind tunnel consisted of a pseudo-2D flat plate which was mounted on a pair of rotary mounting mechanisms on either side of the wind tunnel test section. The flat plate airfoil was made of acrylic and measured $5\frac{3}{16}$ in. (13.18 cm) in chord and 2 ft in span. The leading edge of the flat plate was rounded off in an elliptical fashion to prevent immediate separation at the leading edge. The hot-films used in testing were Dantec DISA 55 R47 sensors and were directly adhered to the surface of the flat plate, without a substrate, positioned around the mid-chord of the plate. Lead wires were soldered directly to the hot-film sensors, routed along the trailing edge of the flat plate, and led out of the wind tunnel to driving circuitry. The rotary gearing mechanism and an inclination sensor were used to finely adjust the angle of attack during testing. Velocity was adjusted manually using a dial controller with velocity read out via display from a Validyne DP15-20 transducer. LabVIEW was used for data acquisition, with a 1 kHz sampling rate for the hot-film sensor, thermocouple, and pressure channels.

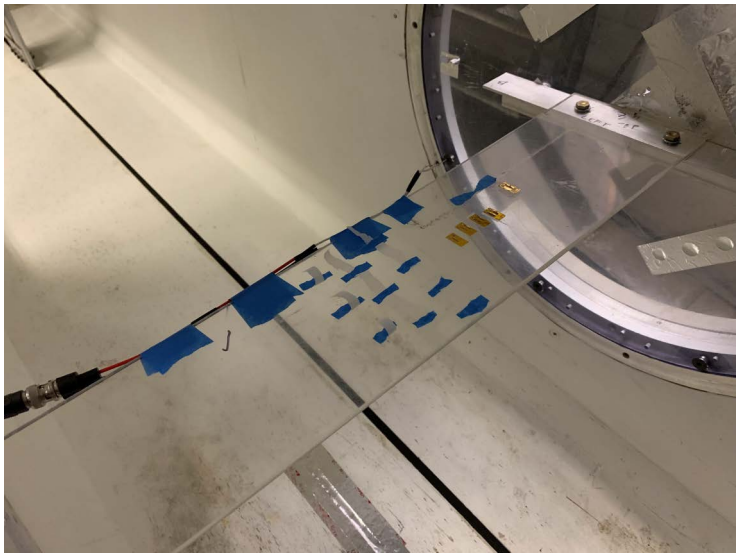

Figure 4.2. The flat plate setup in the closed-loop wind tunnel.

4.2.2 Open-jet Wind Tunnel

The open jet wind tunnel was the facility used for the continuation of CCA and CTA-driven static testing, as well as for the entirety of the unsteady sensor testing. The open jet wind tunnel consisted of an axial air blower, a diffuser housing with multiple screens, a plenum chamber, a high area ratio circular nozzle, and a circular to square transition nozzle with outlet dimensions 8 inches by 8 inches(4). The wind tunnel is shown schematically in figure 4.3. The test section velocity was adjusted via a Dynamatic AF 1500 AC motor controller connected to the wind tunnel blower. The wind tunnel could produce velocities up to 25 m/s, however only velocities up to 15 m/s were used in both static and dynamic testing. In static testing, the tunnel motor controller was set to a constant value while during dynamic tests a function generator was used to provide external inputs to the motor controller to continuously vary the flow speed.

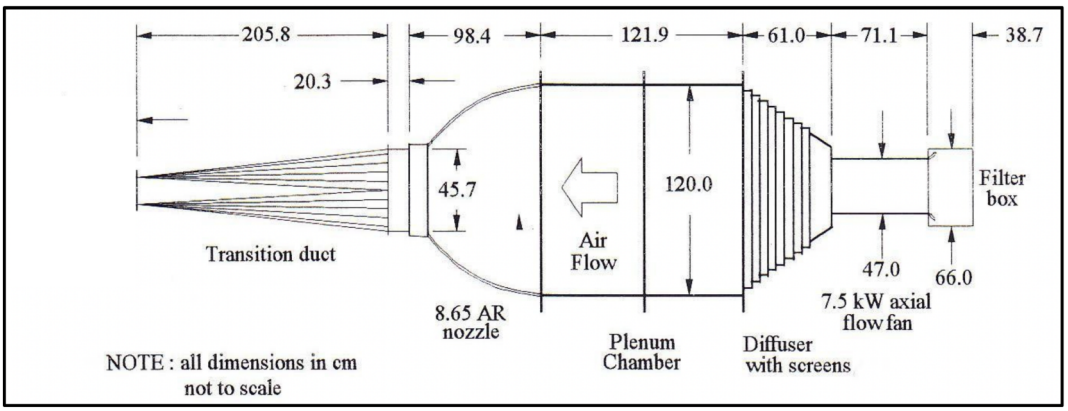

Figure 4.3. Schematic of the open-jet wind tunnel used for static and dynamic testing. Figure reproduced from Town and Camci (4) figure 7.

For the open-jet wind tunnel static testing, a single hot-film and substrate were adhered to an NACA 0012 airfoil. The NACA 0012 used had a chord length, c, of approximately 14.22 cm and was used for static testing, which included angle of attack and wind speed variation. Static validation was accomplished using the fluorescent oil film method. The NACA 0012 was held in place in a cantilevered manner and fixed at the root to a rotary table, which was bolted to a 45-9090 80/20 column. The rotary table enabled fine adjustment of the airfoil angle of attack between experimental runs. Testing in the open-jet wind tunnel utilized hot-film substrates with sensor pads extending to the root of the airfoil. BNC adapter cables were soldered to the solder pads of the substrates and then connected to the data acquisition hardware via BNC cables. The region of the airfoil containing the hot-film and substrate was positioned as close as possible to the centerline of the open-jet wind tunnel outlet in order to minimize turbulent flow and shear effects present near the jet edge. The setup is shown in figure 4.4 and shows a simplified setup with only the cantilevered airfoil, rotary table, and wind tunnel outlet. The tripod in the frame is where the PIV camera was mounted

Figure 4.4. The barebones version of the open-jet wind tunnel setup, containing only the airfoil, rotary table, and wind tunnel outlet.

A pitot-static tube was mounted near the centerline of the wind tunnel exit, clear of the airfoil, to measure wind speed. The pressure difference between total and static ports of the pitot-static tube was measured by a Validyne DP15-26 pressure transducer which output a proportional voltage signal to the data acquisition system. Temperature data was obtained using a type-k thermocouple placed in the flow (Sparkfun part number SEN-13715). A thermocouple amplifier (Sparkfun part number SEN-16294) was used to condition the thermocouple output and had a stated resolution of 0.0625°C. The amplifier communicated with an Arduino board (Sparkfun part number DEV-15123) via the qwiic system, a proprietary i^2c interface. The Arduino board output a proportional voltage signal that was then read in by the main data acquisition system.

The linear hot-film array itself contained three evenly spaced hot-films $\frac{3}{4}$ in (19.05 mm) apart and oriented such that the sensing elements were aligned along the airfoil chord, with no span-wise staggering of the sensors. The hot-film array used can be seen in figure 3.3. The hot-films were individually designated leading edge (LE), mid-chord, and

trailing edge (TE). The hot-film array was driven by the CTA, which was hardware-limited to driving only two individual sensors in the array simultaneously. In unsteady flow testing, one of two combinations of hot-films were driven at a time: the LE and mid-chord, or LE and TE hot-films. The choice of hot-film combination was motivated by the anticipated aerodynamic conditions over the different hot-film sensors, with the LE hot-film primarily experiencing attached flow, the TE hot-film experiencing separated flow, and the mid-chord hot-film experiencing sometimes separated and sometimes attached flows depending on the angle of attack and incoming velocity variations.

Each dynamic test consisted of sinusoidal wind speed variation at a fixed angle of attack. The wind speed variation was commanded via an external function generator, which was connected to both the wind tunnel motor controller as as well as to the data acquisition hardware. For all dynamic tests, the velocity amplitude variation was between 0.5-2 m/s and the frequency of the sine wave ranged from 0.05-0.5 Hz. Combinations of sine wave amplitude and frequency were intended to elicit different aerodynamic conditions over the hot-film array. The function generator was also used to create a repeating, phase-locked square wave which provided the image trigger to the PIV system. The frequency of the trigger signal was adjustable and always phase-locked to the periodic velocity variation.

4.3 Methods of Validation

Methods of validation were needed to in order to relate the hot-film outputs with the true flow over the sensors. Multiple methods of validation were needed to account for static and dynamic testing. Specifically, the fluorescent oil-film method was only valid for static testing, thus PIV was needed for dynamic testing as well as to doubly validate static results.

4.3.1 The Fluorescent Oil-film Method

The fluorescent oil film method was used as a flow visualization method during static testing. It was originally developed by Loving and Katzoff (21) at NASA Langley, and modified by Maughmer and Coder (39) at the Pennsylvania State University. The flow visualization method involved applying a thin layer of fluorescent oil to an airfoil and observing where the thickness of the oil layer was affected by the shearing action of the boundary layer. The method has been shown to reliably indicate regions of flow

separation and laminar separation bubbles (LSBs) (39). To perform the method on the static hot-film experiments, a thin layer of oil was painted onto the surface of the NACA 0012 airfoil in chord-wise strips on either side of the sensor array. The oil mixture was a 3:1 ratio consisting of three parts AeroShell 100W aviation oil, which fluoresced, to one part of a low-viscosity carrier oil, which thinned the mixture. Illumination was provided by an overhead UV light, which created high visual contrast in the oil film. The response of the oil film to wind speed represented the shear at the airfoil surface. Steady state coalescence of the oil film into distinct patterns highlighted structures indicating flow separation and reattachment. Specifically, the structure which indicated separation was a pooling of the oil film, and the structure which indicated re-attachment was an abrupt thinning of the oil layer. Images of these structures were captured using a smartphone positioned above the airfoil, which was triggered manually using a Bluetooth remote. A ruler was placed along the surface of the airfoil to help verify the specific locations of separation and re-attachment. Because the geometry of the NACA 0012 and chord length were known, the arc length s along the surface could be readily converted to normalized x-location x/c. The captured images were post-processed using Adobe Lightroom to make the surface structures and ruler as clear as possible. A visual comparison of the oil film images was then performed to identify the locations of separation and reattachment and to assign a predicted flow condition over the hot-film. With determined flow condition and x/c locations, the oil-film could then be compared with the signal output from the CTA to relate the output to the imaged surface flow. Because the fluorescent oil film method required a steady state condition at the airfoil surface, this method of validation was suitable for static tests only. A sample image of the fluorescent oil method is shown in figure 4.5, which depicts the different structures used to characterize separation and re-attachment, marked by the solid orange and dashed red arrows, respectively.

It is important to note that separation and re-attachment are unsteady phenomena, thus the locations captured by the fluorescent oil film in testing represented only a temporally averaged separation location. The x/c locations of separation and re-attachment varied along the span of the model airfoil. The uncertainties in separation and re-attachment locations were estimated to be a maximum of ± 0.05 x/c, which was determined from the range in the x/c locations of separation and re-attachment lines in the most exaggerated cases. In all cases, the separation location was defined as a line running through the mean separation locations on either side of the sensor array. The oil film method could not be applied over the sensors as it would have affected the heat transfer characteristics and caused errors in the sensor array. A complete fluorescent oil

film data set is available in Appendix A.1.

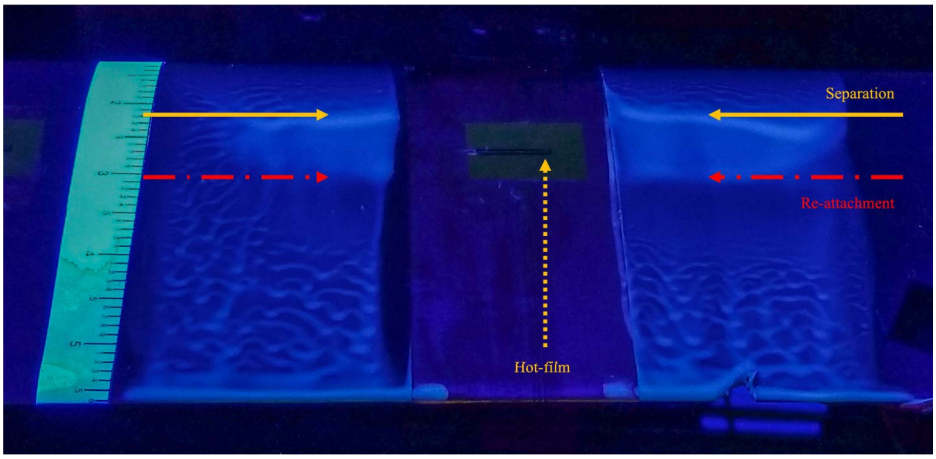

Figure 4.5. An image of the fluorescent oil film method at 8° angle of attack and 14 m/s wind speed. The orange solid arrows indicate the point of separation. The dashed red arrows indicate the the points of re-attachment. The finely dashed orange arrow shows the location of the hot-film sensor.

4.3.2 Particle Image Velocimetry

Particle image velocimetry (PIV) was used to verify hot-film array performance under unsteady inflow. In PIV, the velocity flow fields were constructed statistically by comparing two frames of illuminated particles and calculating the most likely particle path between the two. The time interval between frames and the spatial calibration were known, thus velocity vector fields could be generated. The type of PIV used for validation was planar PIV, here simply PIV, where only a 2D plane of particles was considered for flow quantification.

The PIV system consisted of a Quantel Evergreen2 200 mJ 532 nm dual-pulse laser, an Imager sCMOS CLHS model camera, a LaVision Programmable Timing Unit (PTU-X), and a system PC running the LaVision DaVis 10.1 imaging software. Aerosolized glycerol served as the tracer particle and was generated using a fog machine placed directly in front of the filter box at the inlet of the open-jet wind tunnel. A sheet optic was mounted to the the emitter of the Evergreen2 laser which converted the concentrated laser beam into a laser sheet. The laser sheet was projected wall-normal to the airfoil surface along the chord, as close as possible over the hot-film sensing element(s). In the PIV experimental setup, the airfoil and laser were inverted, with the Evergreen2 laser emitting the laser sheet upwards, and the airfoil positioned such that its nominal upper surface was facing

the ground. This was done for simplicity of setup, so that the laser did not have to elevated. The inverted PIV data could be readily corrected later in post-processing. Images of the illuminated particle fields were captured with the Imager sCMOS camera, which was positioned past the free end of the airfoil. The sCMOS also captured an image of a calibration plate which was positioned in the same plane as the laser sheet in order to load a spatial calibration for processing. The timing of image acquisition was set either in software using the timing box (for the static experiments) or externally triggered using a TTL signal (for the dynamic velocity experiments). Phase-locked data acquisition for the dynamic experiments was accomplished using an external function generator that output pulses at prescribed phases with respect to the sinusoidal motor controller signal.

Preventive measures were taken to reduce laser reflections, where high light intensities could obfuscate the tracer particle information close to the airfoil surface. Flare from reflections could also create false structures in the data. No surface treatments were applied directly to the combined hot-film and copper substrate, which was found to be highly reflective and similar in performance to the mirror finish tested by Paterna et al. (5). The reflective surface of the copper substrate produced superior vector resolution near the surface as compared to an earlier setup which used to a matte black finish. A matte black surface finish was still used to treat the areas surrounding the array hot-film in order to reduce any stray secondary reflections. The matte finish surrounding the array was shown in figure 3.3.

PIV processing was performed using the LaVision DaVis software. The raw images, which were captured directly in DaVis, were loaded directly into the processing pipeline. A series of pre-defined processing actions were applied to the raw images in order to obtain the final vector fields. The specific actions used in DaVis included reflection and background reduction, image pre-processing, and the PIV vector field calculation. The parameters of the PIV processing varied over the course of the experiments and data processing. The final PIV data was processed over three passes of 128 x 128 pixel window, then either three passes of 16 x 16 or 8 x 8 mm windows. Where there were sufficient image samples to compute statistics, the calculated 90 % confidence intervals of the resolved velocities using this processing method were typically less than 0.15 m/s, and nearly confined to the boundary layer. In the outer flow, the uncertainty values were lower, typically less than 0.05 m/s.

Chapter 5
Results and Discussion

5.1 Static Results

5.1.1 CCA Static Results

Initial velocity and angle of attack testing was conducted in the closed-loop wind tunnel using the CCA-driven hot-film. Figure 5.1a shows the averaged output from the CCA-driven hot-film with angle of attack varied from 0-15° at a wind speed of 6.7 m/s measured over a flat plate airfoil with a chord length of 13.18 cm. Over the range of angles of attack, the averaged output voltage was observed to change by 23.5 mV. The direct voltage output from the CCA is plotted in figure 5.1b, which shows that the output from the CCA contained significant noise. The signal-to-noise ratio (SNR)(40) was calculated for this time trace and repeated several times, and it was found to be $SNR = \frac{\mu}{\sigma} \approx 0.8$, where μ and σ were the signal mean and standard deviation respectively. With an SNR of 0.8, the magnitude of the noise was higher than that of the signal, which in the context of hot-film measurements was considered very poor. Despite the poor SNR, averaging the samples for each measurement at each static condition provided a usable mean response with observable static response, as seen in figure 5.1a. Further testing was conducted to evaluate the CCA and sensor combination for changes in wind speed.

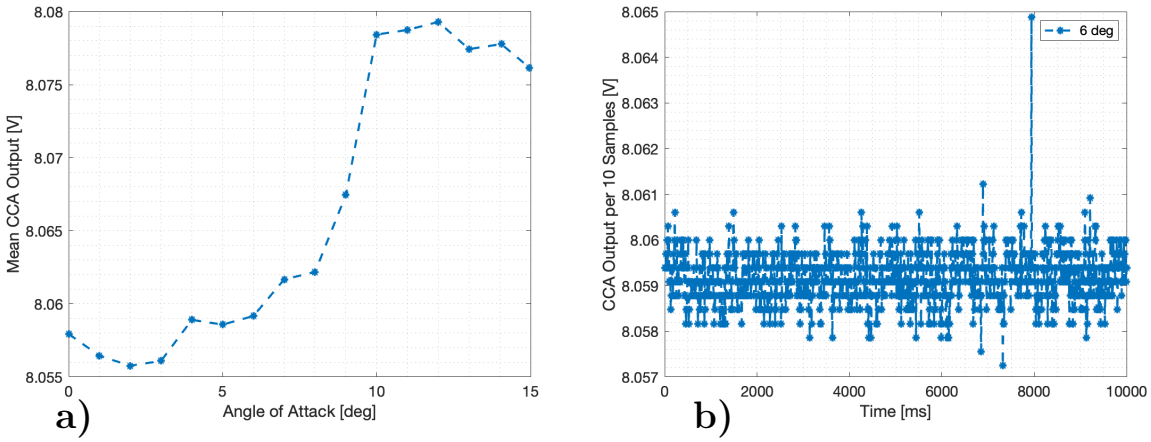

Figure 5.1. The mean output over angles of attack from 0-15°, a, and a time trace of the direct output at 6°, b, are shown for static CCA testing of the hot-film on a flat plate. The noisy direct output in observed in b) was time-averaged to produce a data point in a).

Velocity sweeps were performed for the CCA-driven hot-film. A data set is shown in figure 5.2, which shows an output voltage range of approximately 50 mV for a hot-film attached to the flat plate with wind speed varied over 0-20 m/s. Measurements were taken during both increasing and decreasing wind tunnel velocities to investigate sensor hysteresis. The resulting hysteresis error was relatively large with as much as 20 mV difference being observed between the increasing and decreasing wind speeds. The general trend was that voltages returned to a higher value more quickly during ramp-down of the velocity. Lift and drag experiments using hot films at low chord Reynolds number have demonstrated hysteresis effects (41, 42), which could provide a possible explanation for the effect. Other heat transfer characteristics were also considered such as thermal conduction to the substrate and airfoil, however prior work has shown that conduction damps the frequency response but should not affect the steady-state output(9, 43). Alternatively, because the sensitivity of the CCA output to variation in the ambient temperature, heating of the tunnel over time due to friction losses could also be a possible explanation for the hysteresis. To investigate this, a type-k thermocouple was fixed in the wind tunnel to measure changes in temperature over the duration of the experiment and can be seen in right ordinate in figure 5.2. The thermocouple measured a change in temperature over the course of data collection of $\Delta T = 0.25°\text{C}$, however because the type-k thermocouple only had a specified accuracy of $\pm 0.5°\text{C}$ (44), the measured variation in temperature was assumed to be within margin of error of the thermocouple. However, the hot film does appear to show a strong correlation with temperature, indicating the sensor may be

responding to temperature differences and does not have as strong of a hysteresis effect. This result is encouraging, but does highlight one of the main drawbacks of the CCA, in that the low sensor current makes the hot film much more sensitive to temperature than a traditional CTA circuit. Later results conducted using the CTA showed less sensitivity to temperature and better SNR under similar experimental parameters.

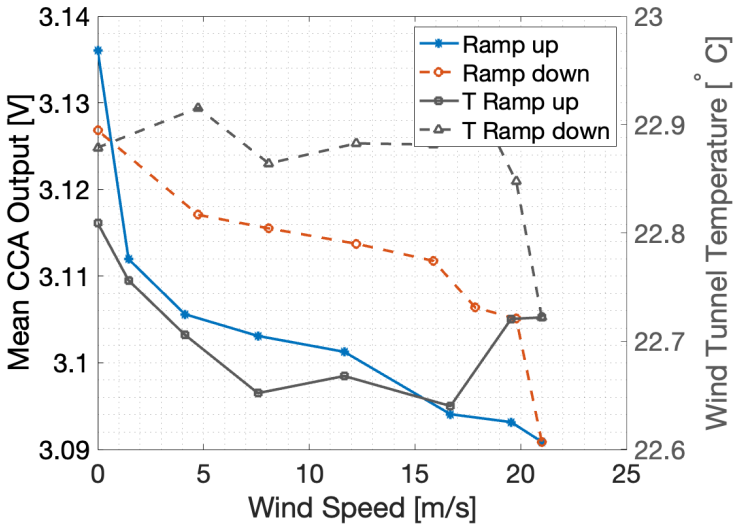

Figure 5.2. The mean voltage output of the CCA for a velocity sweep over wind speeds of 0 to 20 m/s using the baseline configuration of the CCA circuit. A hysteresis error of up to 20 mV was observed for velocities measured during the sweep.

During velocity sweeps, the CCA-driven hot-film sensor was also observed to saturate at high wind speeds. Sensor saturation was a result of the limited joule heating provided by the CCA, where the convective heat transfer of the flow is greater than the joule heating provided to the hot-film sensing element. The saturation of the CCA was considered unacceptable, because the high speeds used during testing, typically a maximum of 20-30 m/s, represented relatively low wind speeds in the applications of interest such at the rotor tips of wind turbines, which are typically greater than 50 m/s, or NLF airfoils, which can extend into the transonic range.

Thus far, a baseline configuration of the CCA had been used, which provided approximately 3 mW of joule heating to the hot-film sensing element. An alternate version of the CCA was built in order to explore solutions to the sensor saturation and hysteresis problems, by sending more power to the hot-film sensing element. The alternate version of the CCA contained a higher reference input voltage to the Wheatstone bridge and lower resistance top resistor within the bridge. The result of the modifications was a

higher current delivered to the hot-film sensor of approximately 7 mW, which would would both increase the output sensitivity and ideally would enable measurement of higher wind speeds before output saturation. The alternate CCA circuit was tested in velocity sweeps and compared to the baseline CCA to evaluate any improvements. Results from velocity testing of the new circuit are shown in figure 5.3 and show increased wind speed sensitivity up to 33 m/s. In addition to better sensitivity, there was a smaller error due to changing ambient temperature of only 10 mV with a total change in voltage of 64.5 mV over the range of velocities tested. The baseline CCA had a hysteresis error as large as 20 mV over a 45.2 mV range for a smaller velocity range of 0-20 m/s.

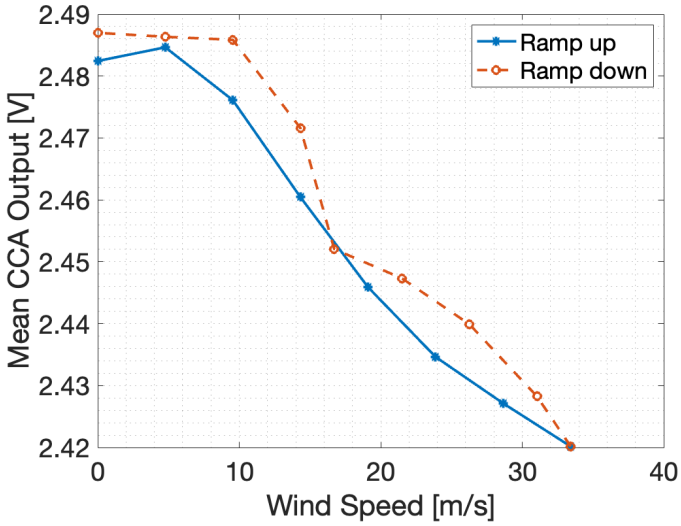

Figure 5.3. The hysteresis loop for the configuration of the CCA with a 20 V reference and 330 Ω top bridge resistors.

Testing of the CCA circuit continued using a new hot-film sensor, new airfoil geometry (the NACA 0012 and NACA 0015) and the open jet wind tunnel. The goal of these tests were to evaluate how the sensor responded on a different substrate more representative of the envisioned application as well as to test the response to more turbulent inflow of the open-jet wind tunnel(4, 45). The DISA 55 R47 hot-film, which was previously used, was replaced by the TaoSystems SF9902, which was a lower cost and more robust hot-film sensor. The SF9902 was also the sensor intended to be incorporated in the large substrate array, whereas the DISA 55 R47 was primarily used for initial testing. In continued static testing, a single SF9902 hot-film was used and mounted at the $x/c = 0.22$ location.

Velocity and angle of attack sweeps performed in the open-jet wind tunnel are shown in figure 5.4 and figure 5.5 respectively. The velocity sweeps using the CCA-driven

hot-film generally did not show a discernible trend in output voltage. Figure 5.4a shows the output voltage between 0-8.5 m/s performed at a -5°. The total voltage output between changing velocities was measured to be approximately 4 mV. Box plots, as shown in figure 5.4b, show that the variation and insensitivity were primarily functions of the noise in the measured signal.

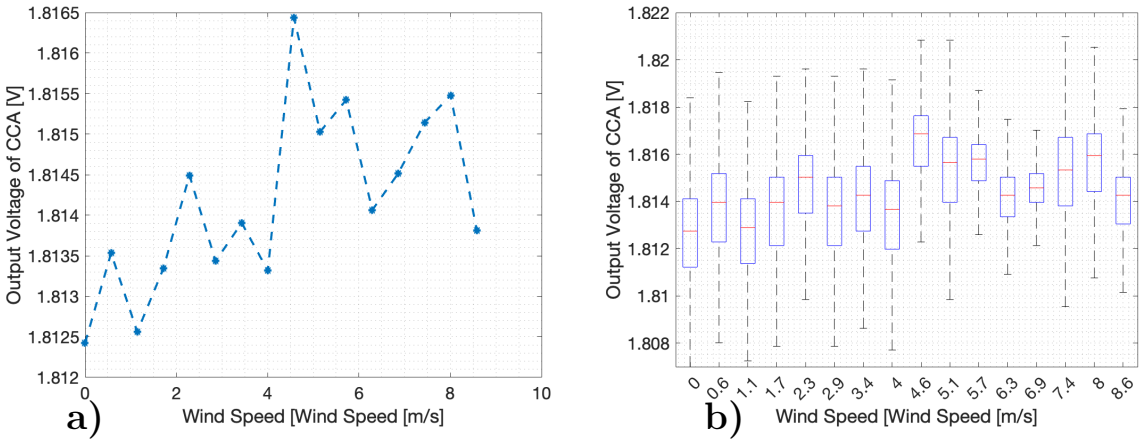

Figure 5.4. The CCA-driven hot-film outputs for 0-8.5 m/s wind speeds at a constant -5° angle of attack. The averaged CCA output voltage by itself is shown, a, as well as box plots containing addition signal data, b.

Additional results were obtained at various angles of attack in the open jet wind tunnel. The sensor did display measurable changes in output over the angle of attack range, similar to the results obtained during testing in the closed-loop wind tunnel. Figure 5.5 shows an angle of attack sweep over -3° to 13° angle of attack at a constant 14 m/s wind speed, with the range of output voltages varying by approximately 30 mV. The box plot shows the variability in the sampled voltages for each angle of attack, which followed the averaged voltage trend unlike in the case of the velocity sweep. The trend in the measured velocities was also consistent with results from CCA-driven velocity testing in the closed-loop wind tunnel, showing a voltage increase as the airfoil angle of attack initially increased as shown in figure 5.1.

The angle of attack experiments in the open jet wind tunnel showed unusual behavior near 2° angle of attack where the sensor output voltage dropped as α was further increased. Validation with the fluorescent oil-film method conducted in sec. CTA Static Results and PIV conducted in sec. Static Validation with PIV would confirm the measured separation at the low angle of attack.

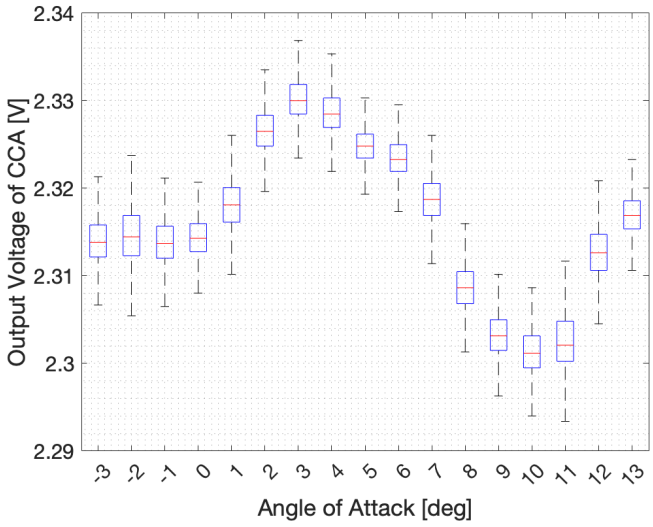

Figure 5.5. The output of the CCA-driven hot-film tested in the the open jet facility for the range of -3° to +13° angle of attack at a constant 14 m/s wind speed.

Because of the unreliable variation in the CCA velocity output and the CCA sensitivity to changes in ambient temperature, it was elected instead to investigate the signal variance to detect the separation condition. The specific quantity used for separation detection was a portion of the frequency domain integrated over the 1-1000 Hz bands. This integrated variance quantity was chosen because of its weaker functional dependence on temperature than flow state. According to work by Stack et al. (14) and Rudmin et al. (22), discussed in chap. 2 on hot-film separation detection, the general signal noise, and thus variance, was expected to increase in transitioning, separated, and turbulent flow compared to nominally attached flow. While Stack et al. (14) found that the most amplified frequency ranges were between 1.0-2.8 kHz, the 1-1000 kHz range was selected with the hot-film in order to account for potentially limited frequency response of the CCA circuit, which operating a hot-film under small power can act like a cold-wire (37). Because this method only measured relative changes in the integrated variance, a velocity or shear stress calibration was not needed (14). The hot-film sensor array resistances did need to be balanced against one another in order to produce consistent circuit outputs.

Figure 5.6 shows the hot-film performance during angle of attack sweeps at 14 m/s wind speeds, for the two CCA circuits test. The integrated variances observed during the angle of attack sweeps showed no discernible trend in the integrated variance as a function of angle of attack. The mean averaged voltages over the angles of attack were overlaid with the integrated variance values as a consistent point of comparison

between the two figures. The experimental parameters were the same as in figure 5.5, which was an angle of attack sweep from -3 to 13° angle of attack acquired at 14 m/s. Figure 5.6a was the output from the higher 20V reference configuration of the CCA, and showed no discernible trend with the reference angle of attack data, with variance values shifting up and down, like the velocity data. Results in figure 5.6b were measured for the baseline CCA and similarly showed no discernible trend. There was an integrated variance increase around the 8° angle of attack, which was later observed to be an angle of attack where the sensor may be exposed to a highly fluctuating flow near boundary layer re-attachment. This increase however, was considered to simply be noise from the CCA, as it was not consistently repeatable.

Several limitations of the CCA circuit have been identified that made it less than ideal as the driving circuit of choice for the hot-film array. Even when attempting to detect bulk changes in flow phenomena (separated versus attached flow), the sensor displayed a low signal-to-noise ratio and was overly sensitive to temperature changes in the flow. Based on prior work, it was anticipated that temperature sensitivity would be a challenge, however attempts to use other statistical measurements of the signal (variance) which were postulated to be less sensitive to temperature were also unsuccessful. Despite the positive practical aspects of the CCA, including low-cost, ease of setup, and dynamic stability (with respect to sensor over-current events) it was elected to employ a CTA circuit with the hot-film array instead. Several of the lessons learned from the CCA were implemented into the CTA-driven array including using the signal variance to quantify flow state.

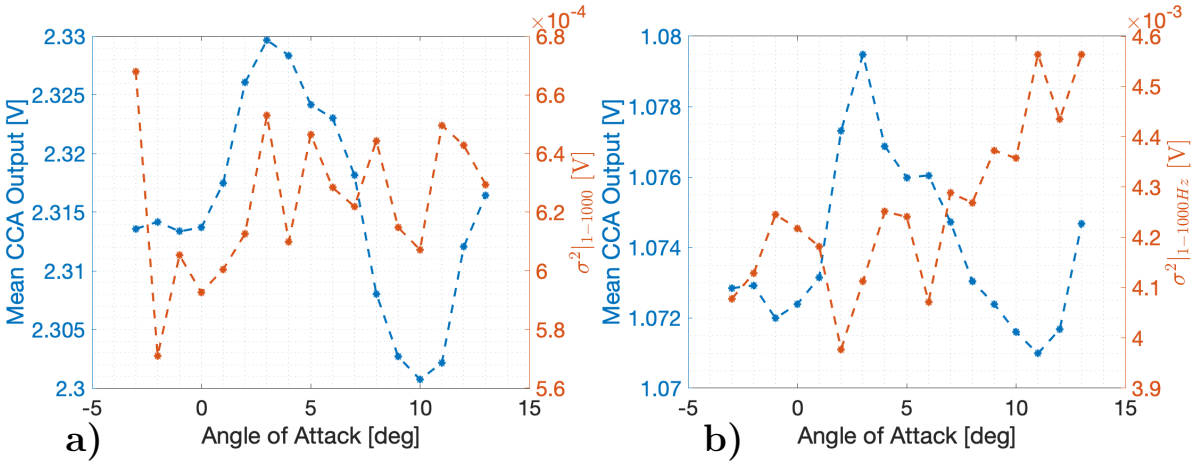

Figure 5.6. Integrated variances are shown over -3 to +13° angle of attack at a constant 14 m/s wind speed. The CCA using the 20 V reference is shown in a, while the baseline CCA is shown in, b. The measured integrated variances were generally not repeatable.

5.1.2 CTA Static Results

CTA-driven testing of the hot-film array was conducted to evaluate the effectiveness of the metrics used to determine the flow state over the sensor. Comparisons of the CTA to the CCA were also made to evaluate relative measurement capabilities. The tests conducted for CTA testing were for similar wind speeds and angles of attack as conducted with the CCA.

Figure 5.7 shows the output of the CTA-driven hot-film at -1 to 7° angles of attack and from 0 to 14.3 m/s wind speeds. The CTA drove the hot-film sensor at an overheat ratio of 0.6, with no filters or gain applied by the IFA 300. This produced a change in the CTA output voltage in the range of 0.3-0.8 V. The CTA showed clear trends with regard to changing velocity and angle of attack, with output voltage decreasing with angle of attack at wind speeds above 1.1 m/s. Asymmetry was observed around 0° angle of attack, where the -1 and +1° cases did not match. In addition, there was variation in the output was observed for the zero velocity case. While the data is presented as angle of attack sweeps at different velocities, the data was collected through velocity sweeps at constant angles of attack. The measured temperature differences between the data sets included in the matrix was measured up to 0.5° C, which was assumed to have influenced the measurements at specific angles of attack, specifically -1° .

Figure 5.8 shows an individual velocity trace from the matrix for a constant 4° angle of attack and velocities ranging from 0-14 m/s. Box plots were created for each data point, which showed typically less than a 0.01 V interquartile range value per measurement. The magnitude of the per measurement interquartile range was similar as compared to the CCA data plotted in fig. 5.5, however the response to changing wind speed was better defined. There was also no observable hysteresis effect in the CTA over the range of angles of attack and velocities, as in the CCA. The CTA did not saturate in the experiments of interest, where the wind speed generally did not exceed 20 m/s.

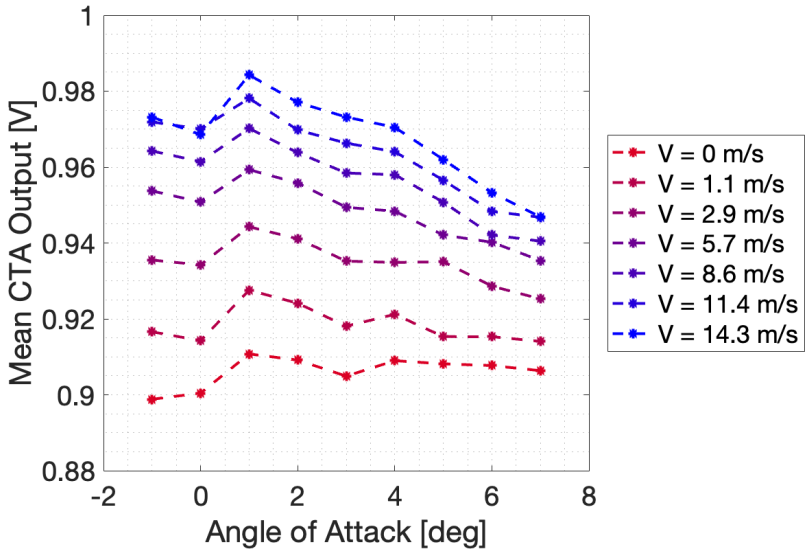

Figure 5.7. The mean CTA output voltage over 0-14.3 m/s wind speed and -1 to +7° angle of attack.

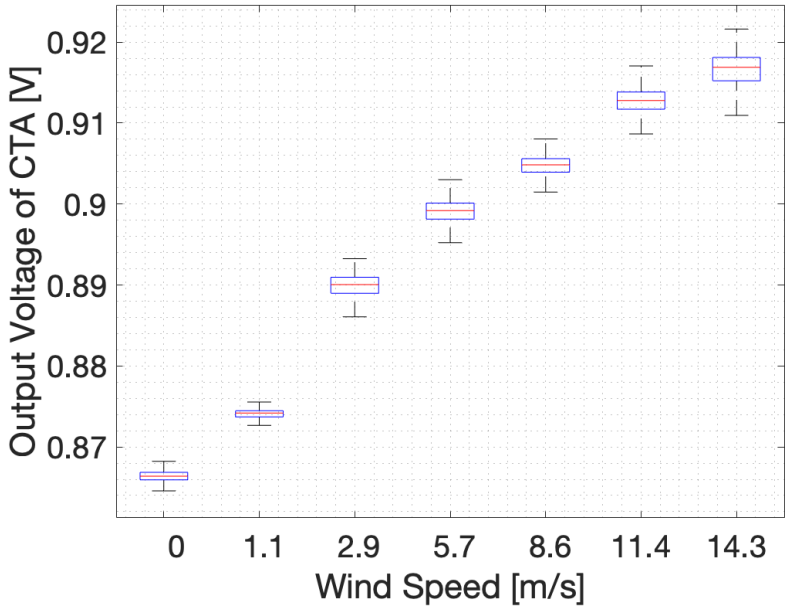

Figure 5.8. The mean CTA output voltage over 0-14.3 m/s wind speed at a constant 4° angle of attack.

Validation of the results from the CTA was performed using the fluorescent oil-film method, which produced a visual representation of the surface flow conditions. A separate set of angle of attack sweeps were conducted concurrently with the oil-film method to

correlate the sensor measurements with the wall shear over the airfoil surface. The oil-film and CTA results are shown in figure 5.10, with a complete set of raw fluorescent oil-film images in Appendix A.1. Figure 5.10a shows the separation and reattachment points indicated by the oil film relative to the location of the hot-film sensor. The oil-film method indicated a separation bubble was almost always present over the sensor up to approximately 11 degrees angle of attack. The presence of a laminar separation bubble was expected due to the relative thickness of the airfoil used and low Reynolds number of the experiment, which was $Re \approx 135,000$. Towards the aft portion of the airfoil, downstream of the hot-film, the flow was observed to re-attach indicated by a sharp dark line. Beyond reattachment, the flow then transitions again and separates as indicated by the turbulent structures starting from the airfoil trailing edge. The structures can be seen in a sample oil-film image below in figure 5.9.

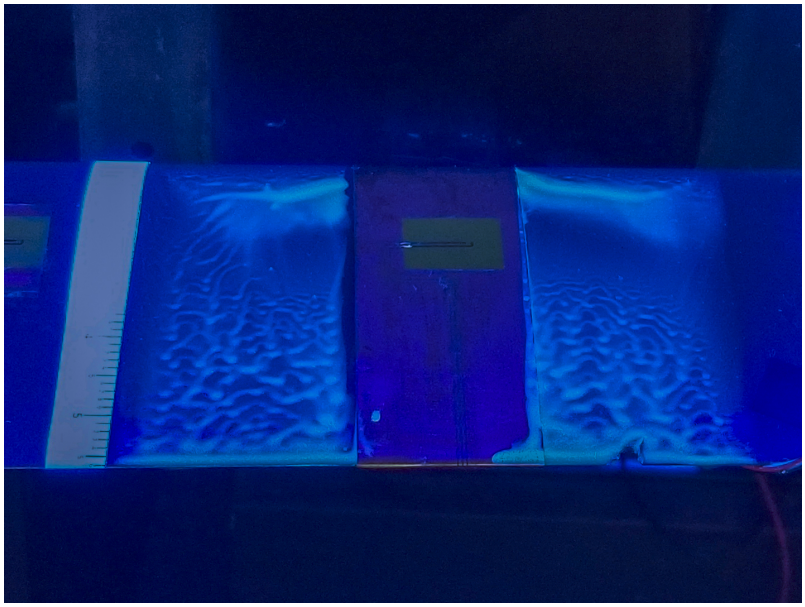

Figure 5.9. A snapshot of the fluorescent oil-film method is shown for a wind speed of 14 m/s at and angle of attack of 12°.

Figure 5.10b shows the signal variance measured by the CTA-driven hot-film, with oil-film separation and re-attachment lines. An arbitrary variance threshold value was set based upon an average of known attached variance values, in order to evaluate the hot-film sensor ability to detect flow. Using this threshold, the sensor detected separation approximately 1 degree after it was indicated by the oil film method and corresponded to a decrease in the signal variance, which was consistent with the literature (14, 22). Following this, near 5° angle of attack the sensor signal spiked and instead recorded

increased variance up to a peak near $\alpha = 9°$. Following this angle of attack, the variance decreased until the oil-film-indicated reattachment zone at approximately 11 degrees α, as shown by the vertical orange line in figure 5.10b.

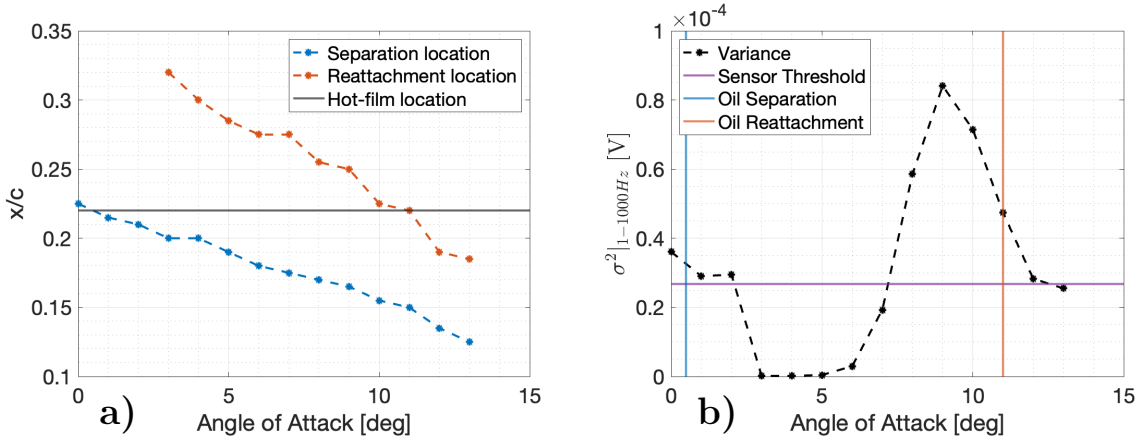

Figure 5.10. The separation location and reattachment location interpreted from the oil-film flow visualization are shown in a) along with the location of the single hot-film element at $x/c = 0.22$. The hot-film signal output variance over a 1-1000 Hz band is shown as a black line in b). Also indicated in b) is the separation and reattachment points from the oil film along with the sensor threshold value for separation detection.

Deduction of the flow state based on the hot-film variance using purely static results was challenging due to both low and high variance values measured in the separated region. The primary limitation of the oil film method was that it only provided static, steady state information on the near-wall flow condition. The increase in the variance was attributed to the action of turbulent mixing injecting additional momentum into the near-wall region, which the oil film method was not able to show. A secondary method of validation using PIV was pursued to gather additional comparison information on the status of the near-wall flow, so that the hot-film sensor behavior could be more clearly interpreted.

5.2 Static Validation with PIV

PIV was used to additionally validate the same static angle of attack sweeps performed using the fluorescent oil-film in order to provide additional information on the region of flow close to re-attachment which was unable to be resolved using the oil-film method. The same experiments were conducted as the oil-film method, namely the angle of attack sweep from 0-13° angle of attack at 14 m/s. The single hot-film substrate used for the

oil-film method was replaced with a hot-film sensor array, with measurements taken using the mid-chord hot-film.

The PIV vector field data was processed to extract the stream-wise and wall-normal velocity components at each point along the surface of the imaged NACA 0012. The maximum standard deviations of the transverse velocity along the airfoil surface was also calculated to estimate a region of transition, which was taken to be associated with the location of separation. The the max transverse standard deviation was adapted from a method which used the maximum RMS velocities to detect transition (33), however the standard deviation was used in order to simplify processing.

The data set taken at a constant 12° angle of attack and 14 m/s wind speed was compared with the results from oil-film, and the velocities resolved by PIV were compared against the max transverse standard deviations to assess the worthiness of the standard deviation metric. The max transverse standard deviations as well as a contour of the velocity magnitude are shown in figure 5.11.

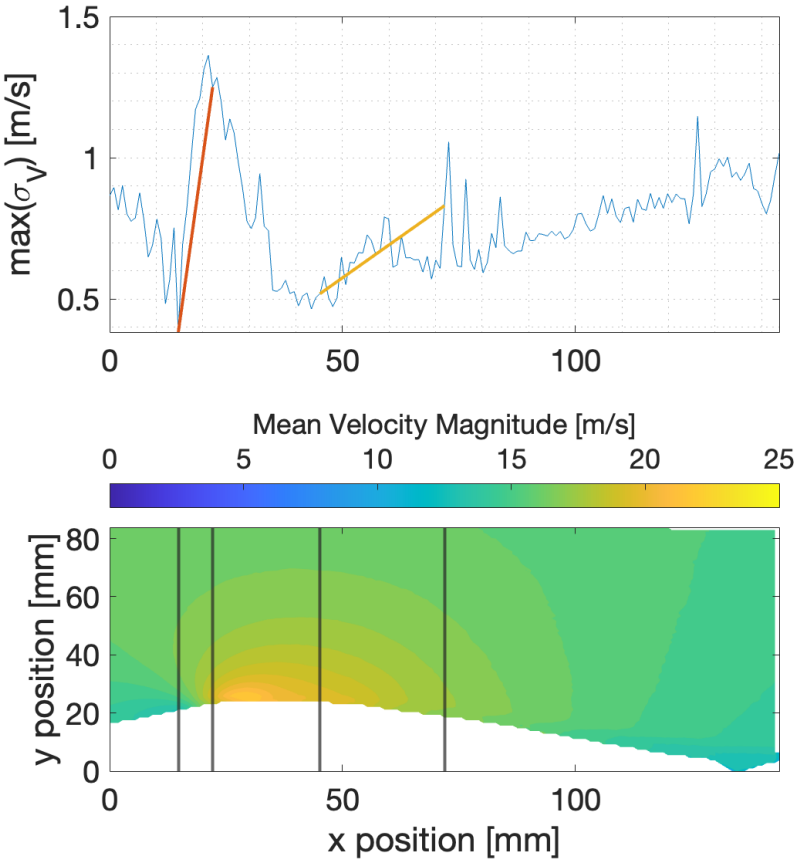

Figure 5.11. The maximum transverse velocity standard deviation plotted against PIV x position and compared with the respective PIV velocity magnitude contour. The increase in the transverse standard deviation is marked as the region of transition.

Immediate inspection of the PIV contour showed agreement in the downstream wake location between the oil-film and the PIV. Upstream, near the leading edge, an increase in the max transverse standard deviations suggested transition. In the maximum transverse standard deviation plot, the increase in the maximum standard deviation is marked with a red line. The bounds of the increase in the transverse standard deviation corresponded to the predicted region of transition. A second increase was observed staring at approximately $x = 50$ mm, which is marked in orange, signified a second transitory region over the airfoil. This was consistent with the oil-film, which showed transition/separation near the leading edge, as well as re-attachment and fluctuations again in the aft portion of the airfoil.

Examination of the velocity profiles, figure 5.12, as well as a static XFOIL simulation (46) showed that the flow separated close to the location of predicted transition.

In figure 5.12, the normalized velocity profiles are shown in addition to a quiver vector field. The velocity profiles were interpolated from the PIV grid to a wall-normal grid utilizing the known airfoil geometry and x positions. In the velocity profile plot, the mean wall-tangential velocities (in m/s) were scaled by a factor 1/100 and added to the x-position to visualize the velocity profiles along the airfoil surface. The velocity profiles were colored red to blue to indicate relative x-position with red being the lowest and blue being the highest.

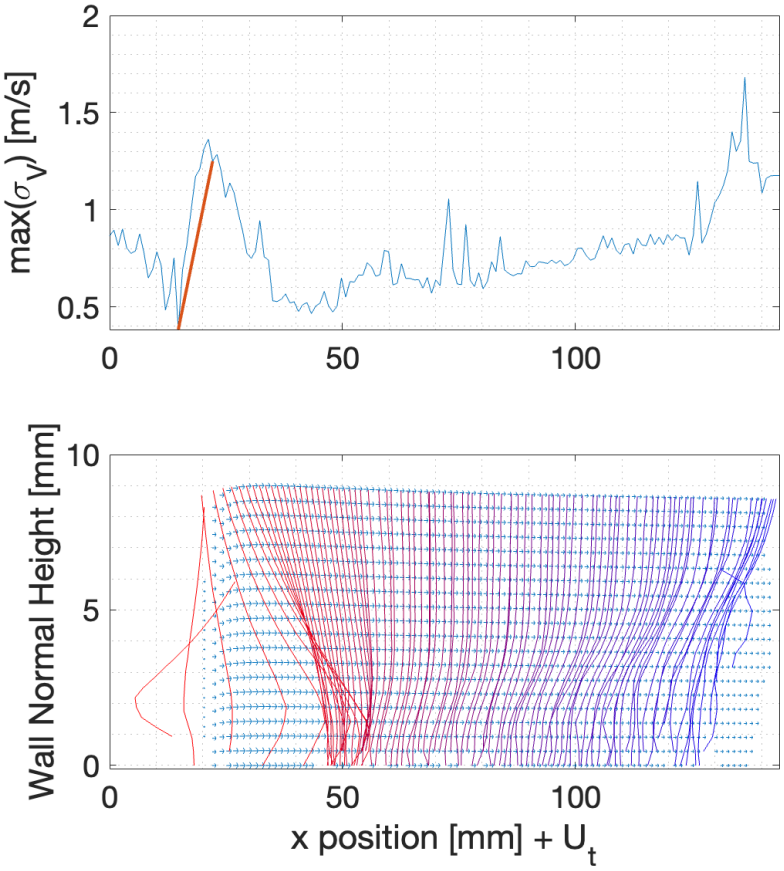

Figure 5.12. The maximum transverse velocity standard deviation plotted against PIV x-position and compared with the velocity profiles in the same region.

Due to the specific combination of the NACA 0012 geometry at 135,000 Reynolds number, unusual separation aerodynamics were observed. Specifically, the flow quickly separated at the leading edge before quickly reattaching and forming a thin boundary layer. This behavior can be seen in the XFOIL results in figure 5.13. Because of the thinner boundary layer near the leading edge, this behavior was not able to be fully

resolved using PIV. Comparing the XFOIL results with PIV data, the PIV was only briefly able to resolve the reverse flow at the leading edge. Instead, the region of accelerated flow just above velocity profile inflection point and reverse flow region was captured, which is shown in the leftmost velocity profile plots in figure 5.12. The PIV data subsequently showed that the flow recovered to a typical velocity profile under an adverse pressure gradient by around $x = 50$ mm ($x/c \approx 0.385$), before separating again downstream near $x = 85$ mm ($x/c \approx 0.65$). These results were also similar to the oil-film results shown in figure 5.10, although the initial region of separation occurred approximately 0.03 x/c ahead for the PIV data set. This can most likely be attributed to the uncertainties of using both methods and effects of the oil-film on the surface geometry of the NACA 0012.

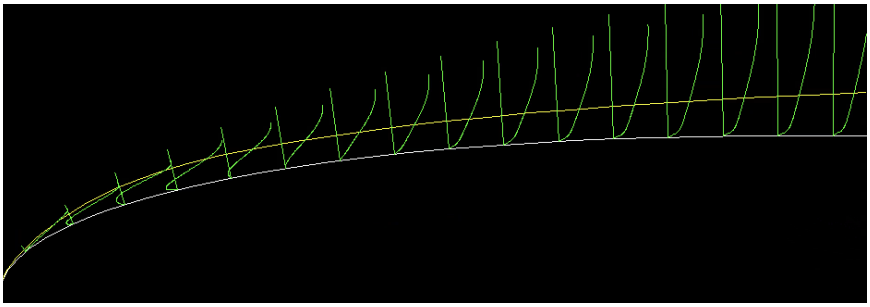

Figure 5.13. XFOIL velocity profile shapes from 0.0 to 0.393 x/c for an NACA 0012 at a constant 12° angle of attack and 14.3 m/s wind speed.

Comparing the PIV, oil-film, and hot-film results appears to confirm that the hot-film sensor was detecting unsteadiness associated with re-attachment. The hot-film location at $x/c = 0.22$ corresponded to the location $x \approx 49$ mm. In the 12° angle of attack case the sensor was within 3 mm of the predicted reattachment zone, which was consistent with the decreasing variances measured by the sensor. This region only showed attached flow in the oil-film images, example in figure 5.9, where unsteadiness was not clearly depicted by the oil.

Another case was examined for a lower 30,000 Reynolds number case, which had better velocity resolution due to a thicker boundary layer. Figure 5.14 shows the maximum transverse velocity standard deviations and mean velocity magnitude contour over an NACA 0015 subject to a 1 m/s wind speed at 15° angle of attack. Like the oil-film data set, initial inspection of figure 5.14 seems to provide a reasonable estimate of the onset of transition and separation.

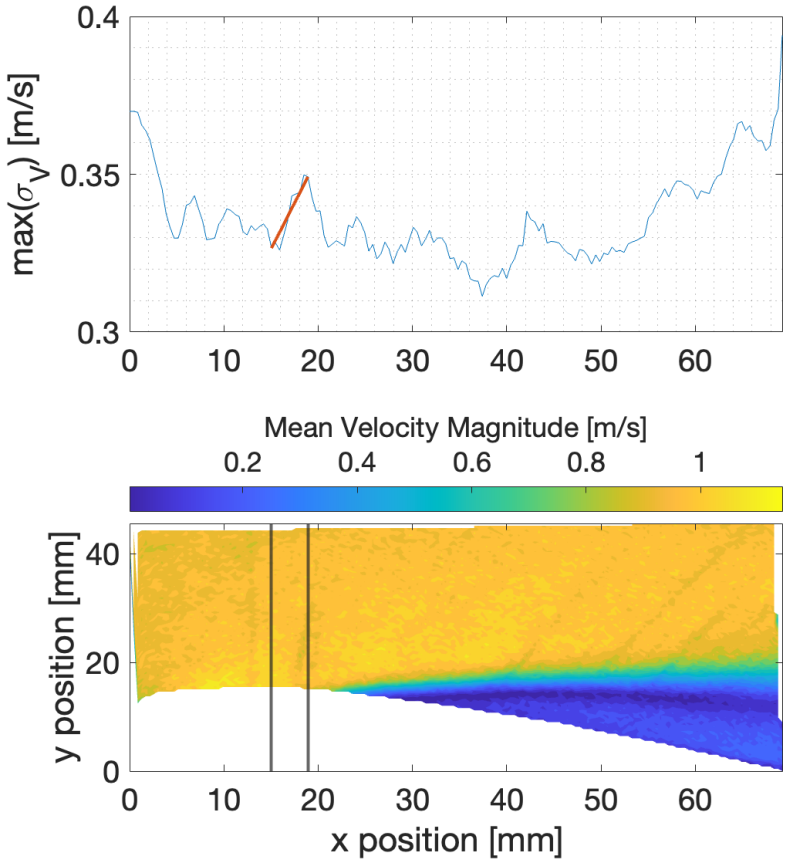

Figure 5.14. The maximum transverse velocity standard deviation plotted against x-position and compared with the respective PIV velocity magnitude contour. The increase in the transverse standard deviation is marked as the region of transition.

A more rigorous examination was then performed using the wall-normal velocities. In this data set, the wall normal velocity profiles were nearly fully resolved and could be used to determine the separation location directly. Figure 5.15 shows the same standard deviation data compared with the velocity field and velocity profiles for the same x positions. In figure 5.15, the boundary layer and velocity profiles can be observed to collapse into a line, which may indicate the boundary between the attach flow and a laminar separation bubble. The same boundary was clearly defined in the previous figure 5.14. The leading edge of the boundary was incident with the latter half of the standard deviation transition range, supporting the use of the max transverse standard deviations as an indicator of flow condition and separation. Reverse flow was measured in this data set due to the low velocity and was first detected shortly behind the shear layer. The quiver plot of the wall-tangential velocity field plotted along with the velocity

profiles shows the same features as the velocity profiles, with both indicating a sharp decline in the velocity past the shear layer boundary and the presence of reverse flow.

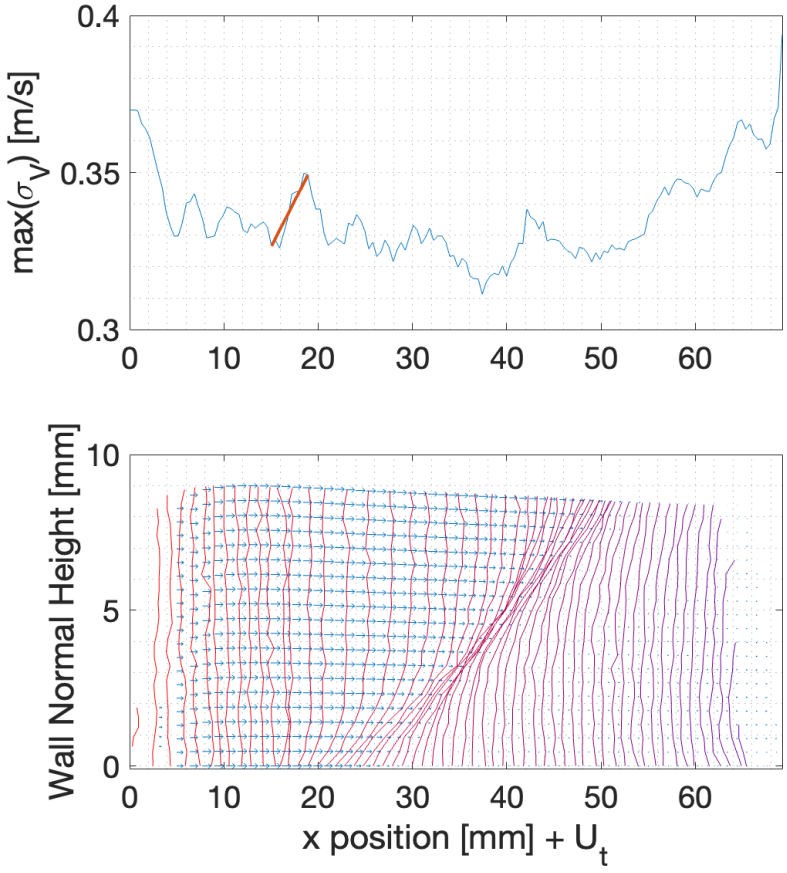

Figure 5.15. The maximum transverse velocity standard deviation plotted against PIV x-position and compared with the velocity profiles in the same region.

Although PIV was not comprehensive in resolving the closest near wall velocities for flow separation detection, examination of the fluctuating transverse velocities (the max transverse standard deviations) further from the wall was used as an indicator for transition and separation. This method generated a range of transition and separation locations used in section 5.4 to evaluate the dynamic testing results. Although the method worked well in deducing the location of separation and reattachment, the method requires a qualitative assessment of the maximum transverse standard deviation increase, which was an objective weakness of the method because it requires a human in the loop. Park et al. (33) quantified the potential error stemming from the qualitative selection of the boundaries as $x/c = \pm 0.02$. Due to the less granular information obtained in

the experiments compared to those of Park et al. (33), the expected error was larger at $x/c = \pm 0.04$, and scales approximately by the PIV resolution. The imprecision in terms of location of separation was not expected to be an issue because the sensor was envisioned as a binary detection method for attached versus separated flow and was not expected to provide insight into the turbulent content of the boundary layer.

5.3 Comparison with Hot-wire

To elicit more information about the near-wall region of flow where there was only very limited resolution with PIV, a comparison was performed between the leading edge hot-film and a single-wire hot-wire in order to compare the voltage outputs and frequency spectra for sample flow conditions. The hot-wire was placed as close as possible to the airfoil surface, within approximately 5 mm, in order to measure the velocity fluctuations in a region near the hot-film. The leading edge hot-film and hot-wire were run concurrently using the CTA, and their outputs were acquired using LabVIEW.

The hot-film and hot-wire sensor direct voltage outputs as well as the integrated variances are shown in figure 5.16 for a static velocity sweep performed over wind speeds from 2.8-14.3 m/s at a constant 11° angle of attack. Due to a difference in overheat ratios chosen (0.45 for the hot-wire and 0.40 for the hot-film) as well as the heat transfer characteristics of each sensors, there was a difference in the magnitude between the mean output voltage and variances for the two sensor outputs over the range of velocities. Despite the difference in direct output magnitude, the hot-film and hot-wire showed a similar trend with respect to velocity, and the integrated variances generally corroborated the expected behavior between the hot-film and hot-wire from static testing, namely an increase in the variance with respect to increasing wind tunnel speed and unsteady events.

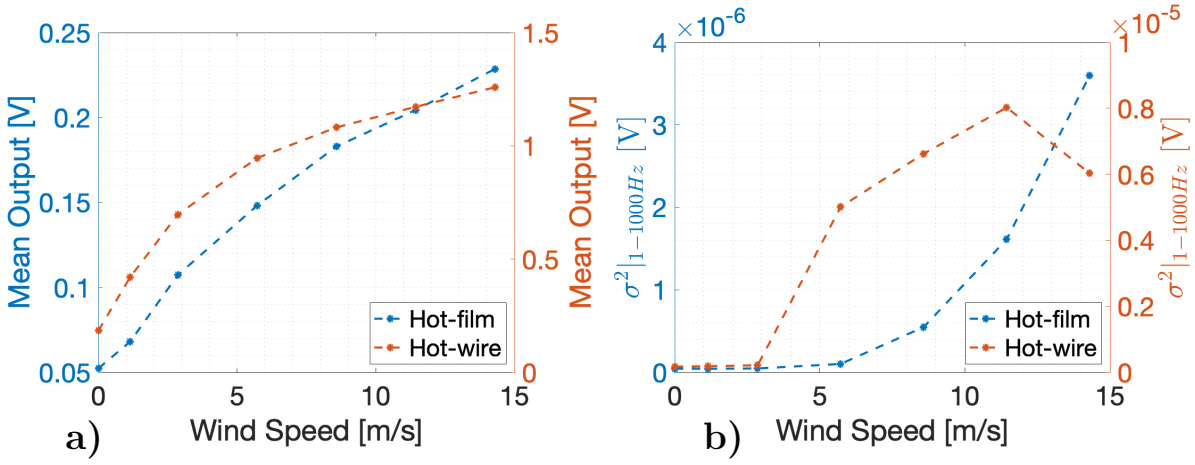

Figure 5.16. Comparison of the hot-wire and hot-film direct voltage outputs and integrated variances for varying wind speed.

In figure 5.16b, the hot-wire consistently output higher variance values, around 10^{-6} V, over the hot-film. Specifically, the hot-wire was able to capture significantly more energy in the higher frequencies which resulted in a higher integrated variance output during the ramp up to higher wind speeds. The pre-multiplied spectra can be seen in figure 5.17 for the same wind speeds of 5.5-14 m/s at a constant 11° angle of attack, which shows that more energy was captured by the hot-wire at the higher frequencies.

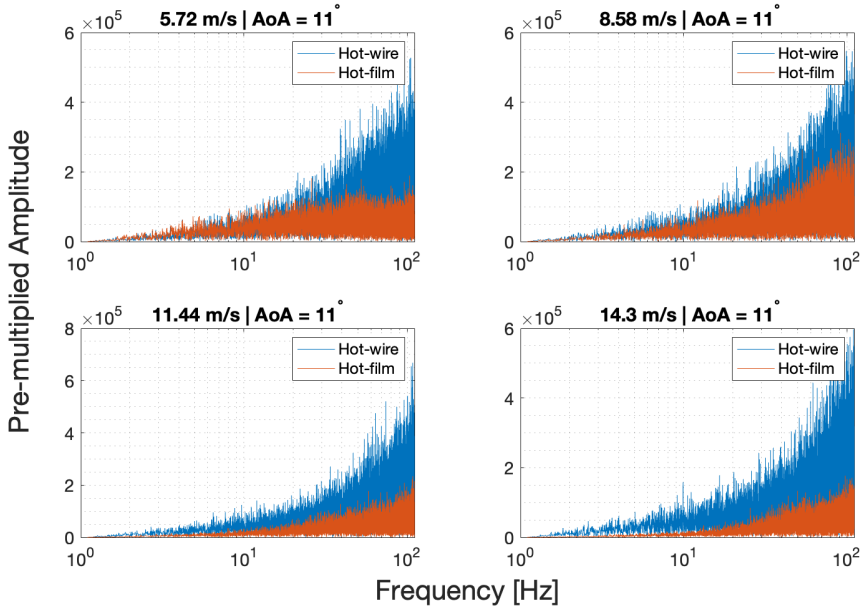

Figure 5.17. Comparison of the hot-wire and hot-film pre-multiplied spectra over 1-1000 Hz for data sets at a constant 11° angle of attack over wind speeds from 2.8-14.3 m/s.

The differences between energy spectra at different wind speeds for both the hot-wire and hot-film were also compared in figure5.18. As velocity increased, both sensors picked up more energy content at higher frequencies. The same trend can be seen in the difference between the 14 m/s and 8.6 m/s cases, however the energy more notably increased for the hot-wire as compared to the hot-film. The hot-film displayed some saturation behavior at high frequencies with an even spread of increasing and decreasing energy content, which is reflected in the variance at the same wind speed in figure 5.16. Although lower in both mean and fluctuating magnitude of the overall output signal, the hot-film did capture similar statistical and spectral trends in the flow as compared to the hot-wire for wind speeds tested below 14 m/s.

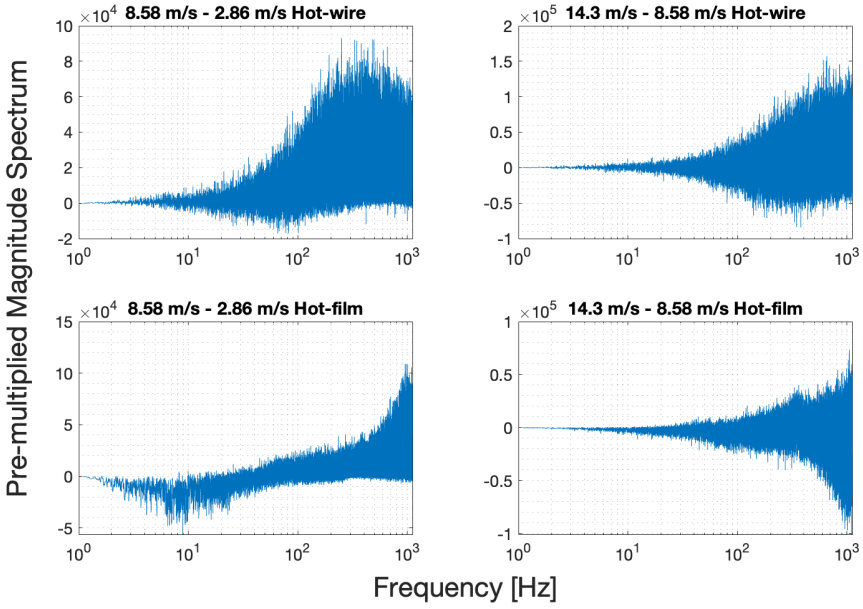

Figure 5.18. Comparison of differences in the hot-wire and hot-film pre-multiplied spectra over 1-1000 Hz for data sets at a constant 11° angle of attack over wind speeds from 2.8-14.3 m/s.

5.4 Dynamic Results

Dynamic testing was conducted to augment the hot-film data collected during static testing. Compared to static testing, the gusting inflow used in dynamic testing was found to produce regions of unsteady flow, which were smaller and harder to detect in static testing. For dynamic testing, hot-film data was acquired from two sensors at a time in a 3-sensor linear array subject to periodic inflow intended to simulate wind gusts. The three hot-films were positioned linearly starting at the leading edge, mid-chord, and then

trailing edge, and were designated as such. For each hot-film measurement, PIV images were captured concurrently to visualize the flow over the hot-film array and measure the velocity field for each phase of the periodic inflow. The wind tunnel variation and the PIV were synced in a phase-locked manner such that ensemble averaged data at phases over the period of variation could be generated.

The hot-film integrated variances were first examined to get an idea of the behavior over the period of variation. Figure 5.19a and figure 5.19b show the integrated variances of the leading edge (LE) and trailing edge (TE) hot-films respectively compared to a pitot-tube positioned at the outlet of the open-jet wind tunnel. The results are for an NACA 0012 at 10° angle of attack subject to a sinusoidal wind speed with an amplitude of approximately 1.5 m/s centered around 3.5 m/s and a frequency of 0.1 Hz. The change in the integrated variance with changing wind speed was readily observed in the case of the LE hot-film, which using the PIV data, was observed to be exclusively exposed to attached flow. The trailing edge hot-film was observed to randomly vary over the phases of the velocity variation, except for a spike in the variance coinciding with the wind tunnel peak velocity. For this data set, the TE hot-film was observed to have operated exclusively in the separated wake, which would explain the lack of a trend in the variance output. This is explored further with PIV results discussed later in this section.

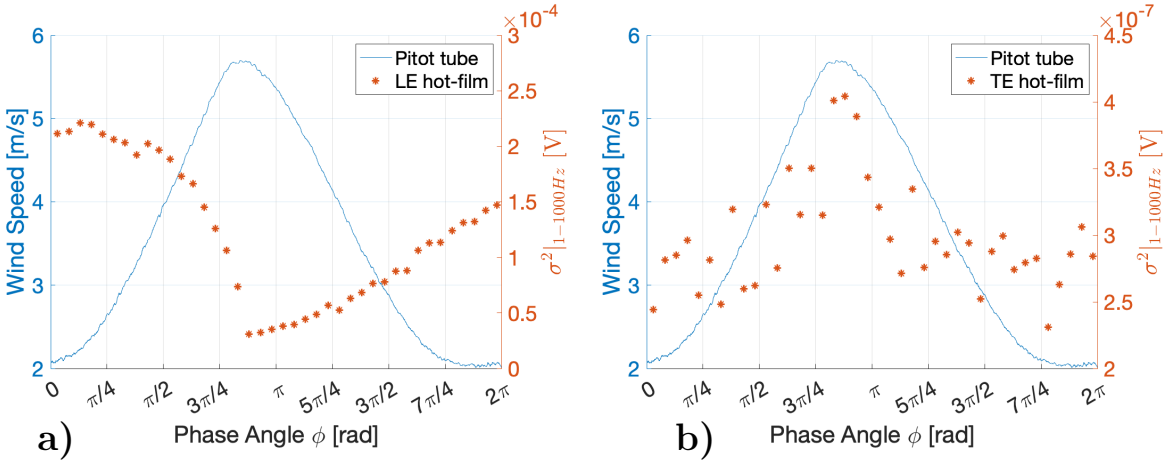

Figure 5.19. The averaged leading edge and trailing edge hot-film integrated variances on an NACA 0012 at 10° angle of attack plotted against the wind tunnel outlet speed for a velocity amplitude of approximately 2 m/s at 0.1 Hz.

The results were similar for another data set using the NACA 0012 at 0° angle of attack where the variation amplitude was reduced to 1 m/s but still centered around 3.5 m/s but at double the frequency at 0.2 Hz. Results are shown in figure 5.20. Similar

integrated variance outputs were observed as in the previous unsteady case in figure 5.19. Namely, there was a sinusoidal trend in the integrated variances with a change in the commanded wind tunnel velocity for the LE hot-film, and randomly varying variances for TE hot-film. In terms of the inspection of the external flow, the LE hot-film was similarly operating under primarily attached flow, whereas the TE hot-film was operating in the separated wake. It is worth noting that the commanded wind tunnel velocity mean and amplitude was actually the same as for the data sets plotted in figures 5.19 and 5.20, however due to the change in gusting frequency and limited ramping response of the wind tunnel motor, the wind tunnel outlet velocity amplitude was reduced by 1/3 in the higher frequency case.

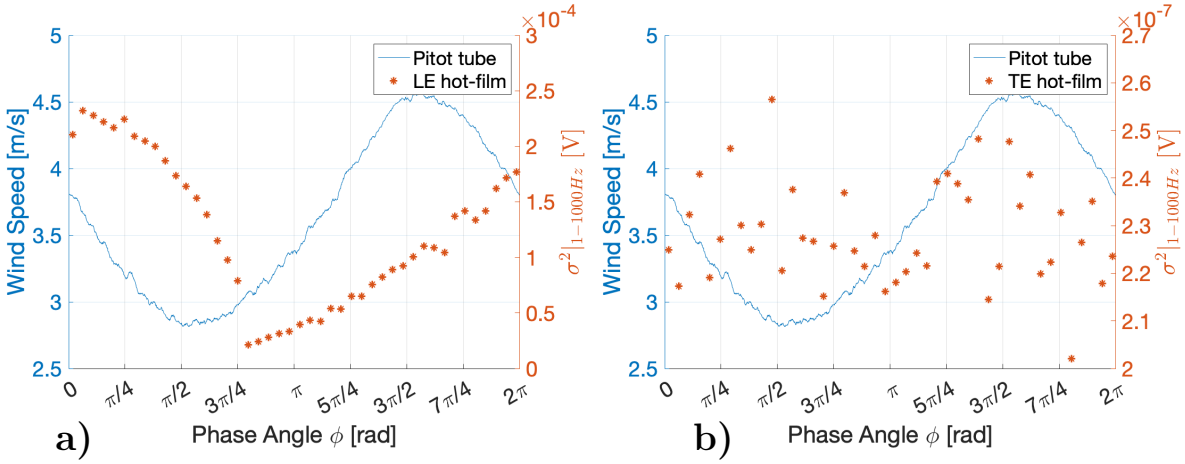

Figure 5.20. The averaged leading edge and trailing edge hot-film integrated variances on an NACA 0012 at 0° angle of attack plotted against the wind tunnel outlet speed for a velocity amplitude of approximately 1 m/s at 0.2 Hz.

A configuration was explored using LE and mid-chord hot-films, with the mid-chord sensor expected to experience a mix of attached, separated, and potentially turbulent flow. Figure 5.21 shows the same type of integrated variance versus wind speed plots for an NACA 0012 at 6° angle of attack with a velocity amplitude of 2 m/s centered around 3 m/s at a frequency of 0.05 Hz. The LE hot-film results were as expected, based upon the results of the previous tests. The mid-chord hot-film experienced mixed results, which showed integrated variances similar to those of separated flow on the order of $10^{-}7$ V, while also showing variation with changing wind tunnel speed. The mid-chord hot-film variance output also showed a more scattered distribution of variances over different phases as compared to the LE hot-film, similar to the behavior of the TE hot-film. There was also a spike in the mid-chord hot-film variance that coincided with the ramp up in

velocity, similar to that seen in figure 5.19b. It is possible that the mid-chord hot-film was primarily in a separated flow region in the phase range of $\pi/2$ and $3\pi/2$ while in other phases outside of this range it was experiencing attached flow. In order to explore the flow behavior over the different hot-films, the PIV-resolved velocity data taken alongside the hot-film measurements was examined.

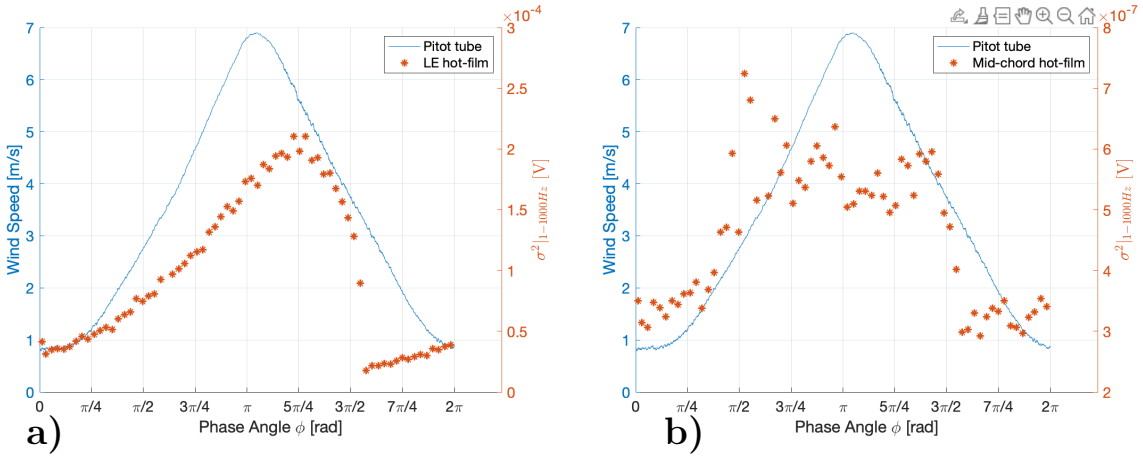

Figure 5.21. The averaged leading edge and mid-chord hot-film integrated variances plotted against the wind tunnel outlet speed for an NACA 0012 with a period of variation for a wind speed amplitude of approximately 1.5 m/s at 0.05 Hz and 6° angle of attack. Here the increase in the variance more closely coincided with the ramp up in wind tunnel velocity.

In comparing the PIV to the hot-film outputs in the unsteady case, specific phases of interest were examined between the PIV flow-field and the hot-film array. The PIV and hot-film data sets were synchronized at the time of acquisition, which produced coupled information between hot-film output and recorded external flow events. The phases chosen for analysis were based upon the hot-film data, particularly phases in the sinusoid where the sensors displayed clear variation in their outputs. The phases in the hot-film output were compared to the same phases from the PIV, which ideally showed differences in the flow corresponding to differences in the hot-film outputs.

Determination of the flow condition was done through analysis of the phase-locked and ensemble averaged PIV velocity vector data near the airfoil surface. Namely, a region was identified where the transverse standard deviation was rapidly increasing. This was the same method discussed in section: Static Validation with PIV . The phases chosen for examination were $\phi = 0$ and $\phi = \frac{5}{4}\pi$, as these phase angles represented low and high variance phases respectively for the mid-chord hot-film output in the data set shown in figure 5.21.

Figure 5.22 shows the PIV data for the same data set as figure 5.21 at the specified $\phi = 0$ and $\phi = \frac{5}{4}\pi$ phases. The primary downstream location of estimated boundary layer transition both started around $x = 57$ mm, however the size of the predicted transition zone varied between the two cases, with the $\phi = 0$ nearly three times larger than that of the $\phi = \frac{5}{4}\pi$ case. In this data set, the mid-cord hot-film was located at $x \approx 79$ mm, which means it was within the designated transition region at both phases.

Based upon the PIV results, it seems likely that the mid-chord hot-film was exposed to a mix of flow conditions over the period of variation. The PIV, which indicated exposure to transition regions of different sizes, potentially suggested that the hot-film may have been exposed predominantly to lower velocity flow in the $\phi = 0$ case, and more unsteady flow in the $\phi = \frac{5}{4}\pi$ case resulting from the increased mixing of the preceding attached flow phase. The LE hot-film, which was located at $x = 40$ mm, appears to have been exposed to primarily attached flow directly from the wind tunnel outlet, with the change in the variance corresponding to the increased energy with respect to increasing wind speed. Unfortunately, the exact condition of the flow was not definitively clear based on the PIV results. This was most likely a combination of the limited PIV resolution near the surface (a larger interrogation region was desired to capture the entire flow over the airfoil), limited samples per ensemble-averaged phase (only a maximum of 18 images per phase were collected versus the suggested minimum samples was 20 images per phase and recommended 30 images (33)), and the application of a static evaluation method to dynamic data. Despite this, some conclusions can still be drawn from the dynamic data. Dynamic testing seems to have confirmed the general behavior observed in static testing, that there was an increase in the hot-film integrated variance with increases in the unsteadiness in the flow. For the data sets taken and analyzed, general magnitudes of the integrated variances fell on the order of 10^{-4} V for attached and unsteady flows and 10^{-6}-10^{-7} V for the low energy flows that can be observed in a separated wake or low velocity recirculation region.

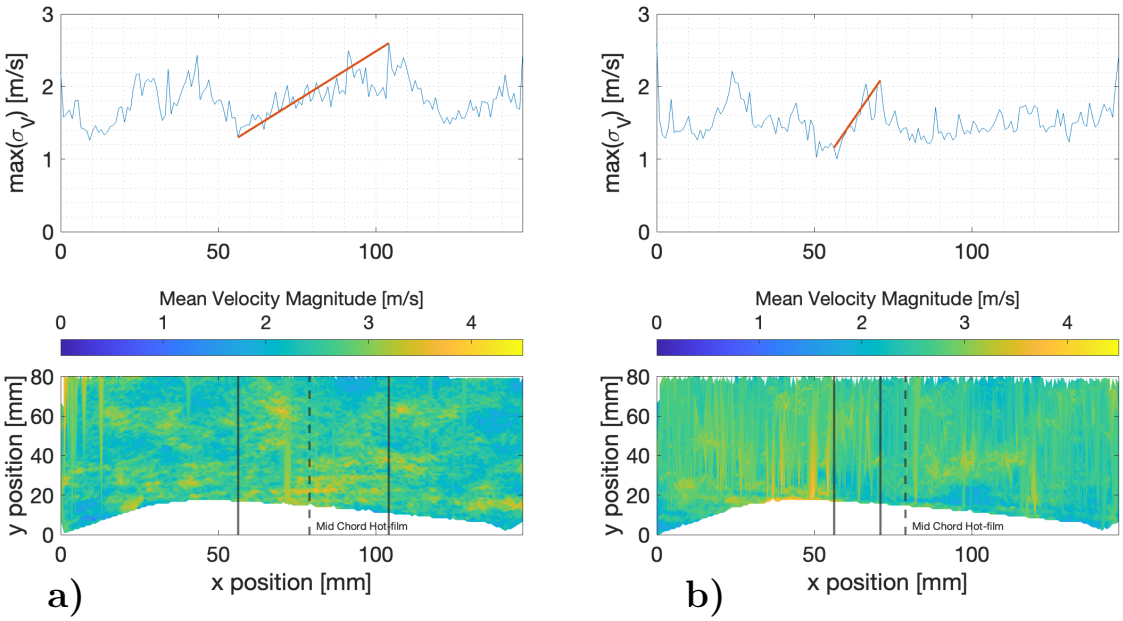

Figure 5.22. The maximum transverse velocity standard deviation over the airfoil as well as the velocity magnitude contours for the NACA 0012 subject to an amplitude of 1.5 m/s at 0.01 Hz and 6° degrees angle of attack. a, is a snapshot at $\phi = 0$, and b is a snapshot at $\phi = \frac{5}{4}\pi$.

Positive and negative phase lags between the pitot-tube and the hot-film outputs were also observed in addition to a consistent hysteresis effect during the decrease in the hot-film output. Whether the hysteresis effect was due to an actual fluid-dynamical phenomena occurring over the airfoil surface during the velocity ramp-down or an artifact of the sensor itself is currently not known. Unfortunately, the PIV also did not capture every detail with respect to these two phenomena, and the causes of either of these effects was ultimately not entirely clear. The phase lags appeared to be a function of the wind speed and variation frequency, and to a smaller extent, the hot-film position and angle of attack. The hysteresis effect appeared closer to the ramp-down of the wind tunnel variation. Movement of the transition region detected earlier, suggested that the hysteresis effect could have been caused by transients in a shifting boundary layer, specifically, a persistence of the energetic flow during decreasing wind speeds after the peak velocity. Ultimately, these effects necessitated finer resolution of the boundary layer and a larger number of averaged samples in order to draw definitive conclusions for dynamic inflow cases.

Chapter 6
Conclusion

6.1 Summary of Findings

The results ultimately showed that the integrated variance metric and PIV used to associate hot-film outputs with flow conditions were successful under static conditions, and in limited capacity, under dynamic conditions for low Reynolds numbers, below 200,000, on an NACA 0012. The method required a circuit with consistent and low noise outputs, which the initially explored CCA could not produce. The IFA 300 CTA, which replaced the CCA, was able to produce the desired signal quality. Consistent with methods discussed in the literature, an increase in the integrated variance of the output of the hot-film sensors could be used to coarsely identify attached and unsteady flow states. Conversely, low integrated variance values were indicative of separated or otherwise very low velocity flow. The attached and unsteady variance values were on the order of 10^{-4} V, and the separated and low velocity variance values were on the order of 10^{-6} - 10^{-7} V. With the SF9902 hot-film sensors driven by the IFA 300 CTA, these values were consistent across all static data sets, and with some uncertainty, the dynamic data sets as well. This also seems to justify the calibration-less method first used by Stack et al. (14), where only knowledge of the relative differences between hot-films outputs or expected voltage outputs were needed.

The fluorescent oil-film was successfully used as a static validation method for identifying initial locations of separation and re-attachment, however it was unable to resolve transient or steady state unsteadiness in the flow. During static testing, the oil-film method and the hot-film reported different results in a region where increased turbulent mixing was suspected. PIV was used, which was able to capture the unsteadiness in the flows, and confirmed that hot-film was measuring increased unsteadiness. By using a method which examined the standard deviations of the transverse velocities, inspired

by work by Park et al. (33), region of transition could be identified. The same method was attempted to be applied to dynamic testing for phase-locked ensemble-averaged PIV. While some trends were visible in the dynamic PIV data sets, the data was not conclusive in comparing both velocity statistics, velocity contours, and the hot-film outputs.

6.2 Limitations and Future Work

Ultimately, not every research objective was met in exploring the hot-film sensor array. While PIV provided useful supplemental velocity data for static testing, more complete data sets for dynamic testing were not obtained due to limited dynamic PIV data sets. A major concern in dynamic PIV and longer data sets was the build up of tracer smoke in the laboratory due to the smoke densities required for PIV. Data sets up to 3 minutes long already created significant smoke, which would have been exacerbated for multiple long data sets. The hot-film was also not able to be tested at the very large Reynolds numbers ($> 10^6$) expected in the proposed applications due to limitations in the chord lengths and wind speeds in the testing facilities. Similarly, the gusting simulations in dynamic testing were constrained either to low amplitude or low frequency variation due to the finite ramping rate of the wind tunnel motor, which was also not representative of the magnitudes of variation that may occur in the field.

Future work would focus on refining the experiments conducted with the hot-film sensors, including design space explorations for wind speeds, Reynolds numbers, and PIV interrogation regions for better flow characterization. The current results provided a exploratory initial characterization of the hot-film output for different flows. Testing of the hot-film array in either the field or in a facility more capable of reproducing higher Reynolds number would be an interesting next step to explore if the sensor performs the same under more realistic conditions. Lastly, an exploration of a re-made low-cost CCA and a new low-cost CTA, which could re-open the doors for the scalable aspect of the initial project. A new CCA and new CTA were developed as part of the Capstone project of an undergraduate research assistant. Initial testing of circuits showed sensitivity comparable to the IFA 300, however the circuits were not completed in time to be included in this thesis.

Appendix A
Fluorescent Oil Film Images over Angles of Attack

A.1 **a)** $\alpha = 0°$

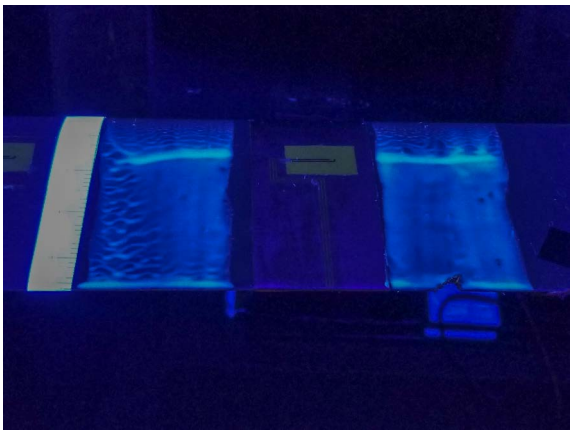

A.1 **b)** $\alpha = 1°$

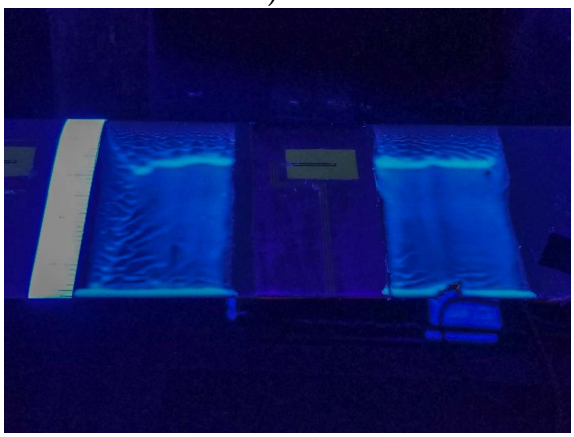

A.1 **c)** $\alpha = 2°$

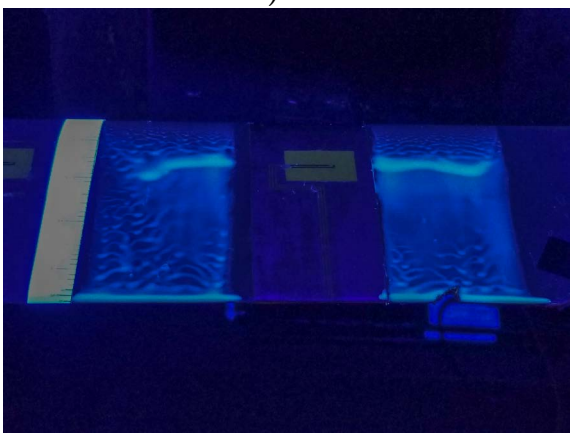

A.1 **d)** $\alpha = 3°$

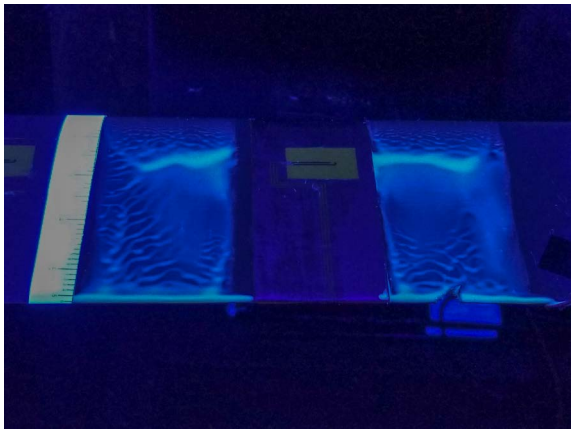

A.1 **e)** $\alpha = 4°$

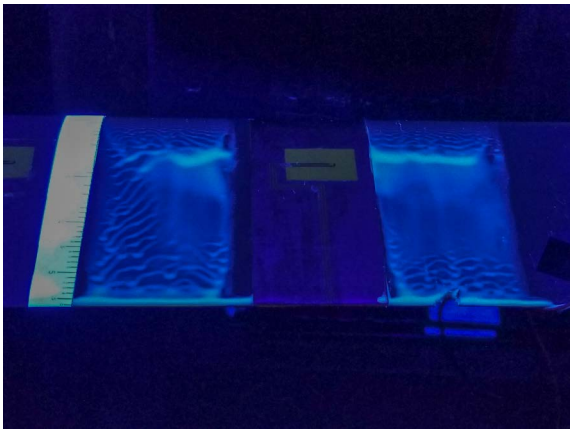

A.1 **f)** $\alpha = 5°$

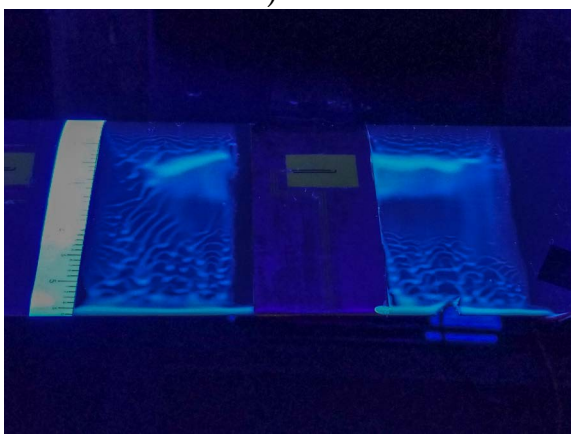

A.1 **g)** $\alpha = 6°$

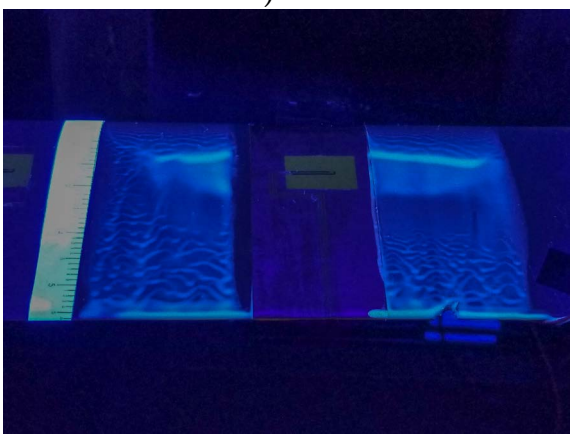

A.1 **h)** $\alpha = 7°$

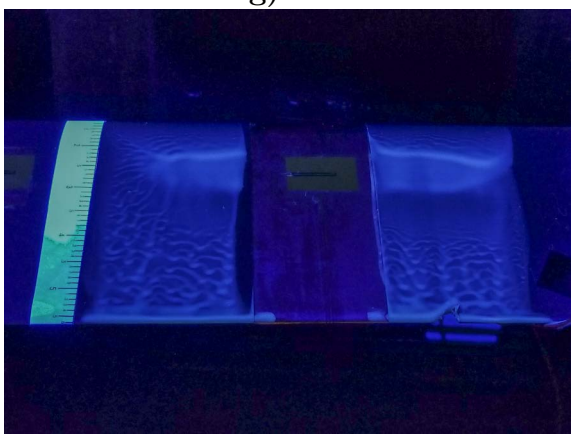

A.1 **i)** $\alpha = 8°$

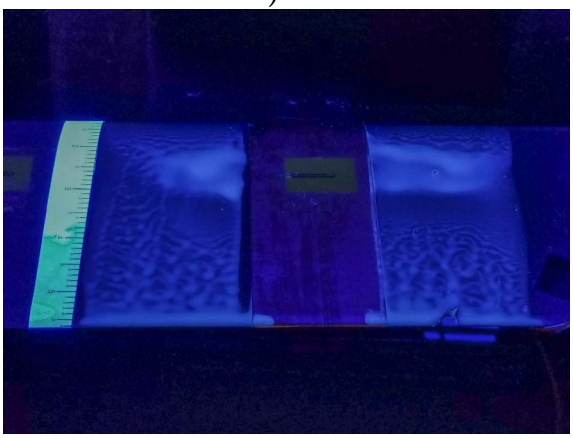

A.1 **j)** $\alpha = 9°$

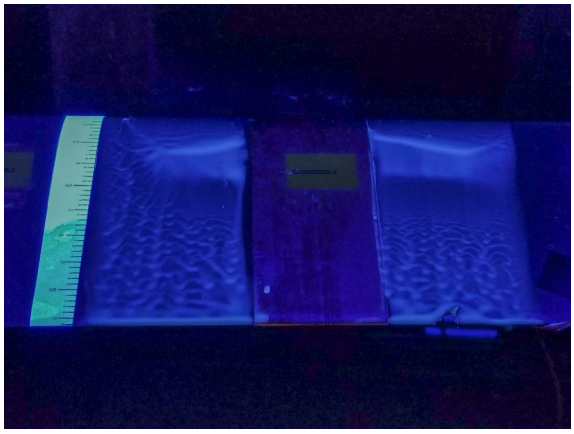

A.1 **k)** $\alpha = 10°$

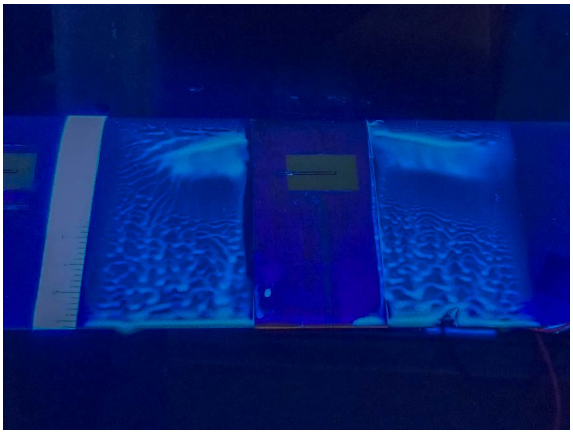

A.1 **l)** $\alpha = 11°$

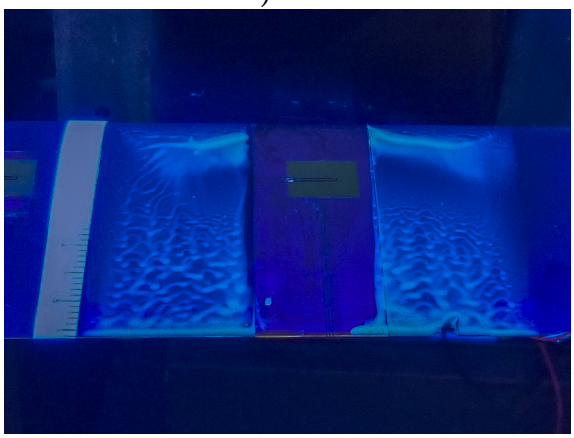

A.1 **m)** $\alpha = 12°$

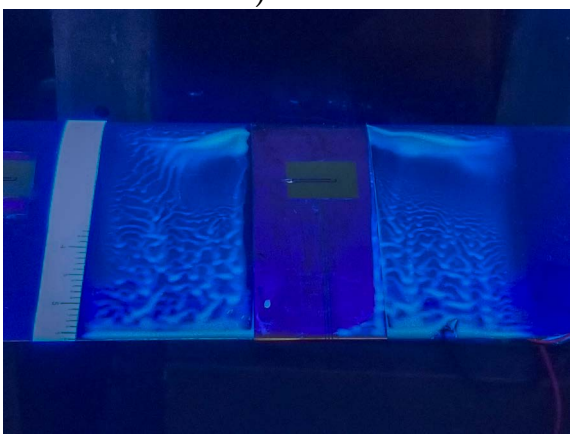

A.1 **m)** $\alpha = 13°$

Figure A.1. The fluorescent oil film method is shown above, with A.1a-m) corresponding to the range of angles of attack from 0-13 ° at a constant 14 m/s wind speed. The hot-film sensing is located at approximately $x/c = 0.22$ and can be seen as the dark line contained in the yellow rectangle. The separation location is marked the leading edge of pooling of the fluorescent oil. The reattachment location is indicated by a darker region directly after the pooled oil, where the reattached flow has blown away the oil. A ruler is applied to the airfoil which corresponds to the arc length over the surface.

Bibliography

[1] Figliola, R. S., and Beasley, D. E., *Theory and design for mechanical measurements*, John Wiley & Sons, 2020.

[2] Buckney, N., Pirrera, A., Green, S. D., and Weaver, P. M., "Structural efficiency of a wind turbine blade," *Thin-Walled Structures*, Vol. 67, 2013, pp. 144–154.

[3] of Systems Integration Inc., T., "Multi-Element Surface Hot-Film Sensors," Online, June 2023. URL `https://www.taosystem.com/products/senflex/senflex.pdf`.

[4] Town, J., and Camci, C., "Sub-miniature five-hole probe calibration using a time efficient pitch and yaw mechanism and accuracy improvements," *Turbo Expo: Power for Land, Sea, and Air*, Vol. 54631, 2011, pp. 349–359.

[5] Paterna, E., Moonen, P., Dorer, V., and Carmeliet, J., "Mitigation of surface reflection in PIV measurements," *Measurement science and technology*, Vol. 24, No. 5, 2013, p. 057003.

[6] Bruun, H. H., "Hot-wire anemometry: principles and signal analysis," *Measurement Science and Technology*, Vol. 7, No. 10, 1996, p. 024.

[7] Comte-Bellot, G., "Hot-wire anemometry," *Annual review of fluid mechanics*, Vol. 8, No. 1, 1976, pp. 209–231.

[8] Liepmann, H. W., and Skinner, G. T., "Shearing-stress measurements by use of a heated element," 1954.

[9] Bellhouse, B., and Schultz, D. L., "Determination of mean and dynamic skin friction, separation and transition in low-speed flow with a thin-film heated element," *Journal of Fluid Mechanics*, Vol. 24, No. 2, 1966, pp. 379–400.

[10] Ling, S.-c., *Measurement of flow characteristics by the hot-film technique*, The University of Iowa, 1955.

[11] Bankoff, S., and Rosler, R., "Constant-Temperature Hot-Film Anemometer as a Tool in Liquid Turbulence Measurements," *Review of Scientific Instruments*, Vol. 33, No. 11, 1962, pp. 1209–1212.

[12] Seed, W., and Wood, N., "Velocity patterns in the aorta," *Cardiovascular research*, Vol. 5, No. 3, 1971, pp. 319–330.

[13] Owen, F. K., "Transition experiments on a flat plate at subsonic and supersonic speeds," *AIAA Journal*, Vol. 8, No. 3, 1970, pp. 518–523.

[14] Stack, J., Mangalam, S., and Berry, S., "A unique measurement technique to study laminar-separation bubble characteristics on an airfoil," *19th AIAA, Fluid Dynamics, Plasma Dynamics, and Lasers Conference*, 1987, p. 1271.

[15] Lee, T., and Basu, S., "Measurement of unsteady boundary layer developed on an oscillating airfoil using multiple hot-film sensors," *Experiments in Fluids*, Vol. 25, No. 2, 1998, pp. 108–117.

[16] of Energy, U. D., "U.S. Department of Energy's Strategy to Advance Offshore Wind Energy in the United States," Press Release, 2023. URL `https://www.energy.gov/eere/us-department-energys-strategy-advance-offshore-wind-energy-united-states`.

[17] Steers, L. L., "Natural laminar flow flight experiment," *NASA. Langley Research Center Advan. Aerodyn. and Active Controls*, 1981.

[18] Poggie, J., Tilmann, C. P., Flick, P. M., Silkey, J. S., Osbourne, B. A., Ervin, G., Maric, D., Mangalam, S., and Mangalam, A., "Closed-loop stall control system," *Journal of Aircraft*, Vol. 47, No. 5, 2010, pp. 1747–1755.

[19] Chabert, T., Dandois, J., and Garnier, É., "Experimental closed-loop control of flow separation over a plain flap using slope seeking," *Experiments in fluids*, Vol. 55, 2014, pp. 1–19.

[20] Sewall, W., Stack, J., McGhee, R., and Mangalam, S., "A New Multipoint Thin-Film Diagnostic Technique for Fluid Dynamic Studies," Tech. rep., SAE Technical Paper, 1988.

[21] Loving, D. L., and Katzoff, S., "The Fluorescent-Oil Film Method and Other Techniques for Boundary-Layer Flow Visualization," Tech. rep., 1959.

[22] Rudmin, D., Benaissa, A., and Poirel, D., "Detection of laminar flow separation and transition on a NACA-0012 airfoil using surface hot-films," *Journal of Fluids Engineering*, Vol. 135, No. 10, 2013.

[23] Kolmogorov, A. N., "The local structure of turbulence in incompressible viscous fluid for very large Reynolds numbers," *Proceedings of the Royal Society of London. Series A: Mathematical and Physical Sciences*, Vol. 434, No. 1890, 1991, pp. 9–13.

[24] Schreivogel, P., "Detection of laminar-turbulent transition in a free-flight experiment using thermography and hot-film anemometry," ????

[25] Hausmann, F., and Schroder, W., "Coated hot-film sensors for transition detection in cruise flight," *Journal of Aircraft*, Vol. 43, No. 2, 2006, pp. 456–465.

[26] Sturm, H., Dumstorff, G., Busche, P., Westermann, D., and Lang, W., "Boundary layer separation and reattachment detection on airfoils by thermal flow sensors," *Sensors*, Vol. 12, No. 11, 2012, pp. 14292–14306.

[27] Buder, U., Petz, R., Kittel, M., Nitsche, W., and Obermeier, E., "AeroMEMS polyimide based wall double hot-wire sensors for flow separation detection," *Sensors and Actuators A: Physical*, Vol. 142, No. 1, 2008, pp. 130–137.

[28] King, L. V., "XII. On the convection of heat from small cylinders in a stream of fluid: Determination of the convection constants of small platinum wires with applications to hot-wire anemometry," *Philosophical transactions of the royal society of London. series A, containing papers of a mathematical or physical character*, Vol. 214, No. 509-522, 1914, pp. 373–432.

[29] Jørgensen, F., "How to measure turbulence with hot-wire anemometers - a practical guide," 2002.

[30] Hultmark, M., and Smits, A. J., "Temperature corrections for constant temperature and constant current hot-wire anemometers," *Measurement Science and Technology*, Vol. 21, No. 10, 2010, p. 105404.

[31] Sun, B., Ma, B., Luo, J., Li, B., Jiang, C., and Deng, J., "Sensing elements space design of hot-film sensor array considering thermal crosstalk," *Sensors and Actuators A: Physical*, Vol. 265, 2017, pp. 217–223.

[32] Burgmann, S., Dannemann, J., and Schröder, W., "Time-resolved and volumetric PIV measurements of a transitional separation bubble on an SD7003 airfoil," *Experiments in fluids*, Vol. 44, 2008, pp. 609–622.

[33] Park, D., Shim, H., and Lee, Y., "PIV measurement of separation bubble on an airfoil at low Reynolds numbers," *Journal of Aerospace Engineering*, Vol. 33, No. 1, 2020, p. 04019105.

[34] Wynnychuk, D. W., and Yarusevych, S., "Characterization of laminar separation bubbles using infrared thermography," *AIAA Journal*, Vol. 58, No. 7, 2020, pp. 2831–2843.

[35] Sun, B., Wang, P., Luo, J., Deng, J., Guo, S., and Ma, B., "A flexible hot-film sensor array for underwater shear stress and transition measurement," *Sensors*, Vol. 18, No. 10, 2018, p. 3469.

[36] Pang, P., Ma, B., Zhang, Z., Luo, J., and Deng, J., "Influence of Size Effect on Dynamic Characteristics of Hot-film Wall Shear Stress Sensor," *2022 IEEE Sensors*, IEEE, 2022, pp. 1–4.

[37] Tsuji, T., Nagano, Y., and Tagawa, M., "Frequency response and instantaneous temperature profile of cold-wire sensors for fluid temperature fluctuation measurements," *Experiments in Fluids*, Vol. 13, No. 2-3, 1992, pp. 171–178.

[38] Horlock, J., "Fluctuating lift forces on aerofoils moving through transverse and chordwise gusts," 1968.

[39] Maughmer, M. D., and Coder, J. G., "Comparisons of theoretical methods for predicting airfoil aerodynamic characteristics," Tech. rep., AIRFOILS INC PORT MATILDA PA, 2010.

[40] Smith, S. W., et al., "The scientist and engineer's guide to digital signal processing," , 1997.

[41] Mueller, T. J., "The influence of laminar separation and transition on low Reynolds number airfoil hysteresis," *Journal of Aircraft*, Vol. 22, No. 9, 1985, pp. 763–770.

[42] Yang, Z., Igarashi, H., Martin, M., and Hu, H., "An experimental investigation on aerodynamic hysteresis of a low-Reynolds number airfoil," *46th AIAA aerospace sciences meeting and exhibit*, 2008, p. 315.

[43] Menendez, A., and Ramaprian, B., "The use of flush-mounted hot-film gauges to measure skin friction in unsteady boundary layers," *Journal of Fluid Mechanics*, Vol. 161, 1985, pp. 139–159.

[44] *DP25-TC AND DP25B-TC Programmable Digital Thermocouple Meter*, Omega, 2019. URL `https://assets.omega.com/manuals/M3732.pdf`.

[45] Uzol, O., and Camci, C., "The effect of sample size, turbulence intensity and the velocity field on the experimental accuracy of ensemble averaged PIV measurements," *4th International Symposium on Particle Image Velocimetry*, Vol. 69, 2001.

[46] Drela, M., "XFOIL: An analysis and design system for low Reynolds number airfoils," *Low Reynolds number aerodynamics*, Springer, 1989, pp. 1–12.